A&A, 682, A151 (2024)
https://doi.org/10.1051/0004-6361/202346463

Astronomy & Astrophysics

A soft and transient ultraluminous X-ray source with six-hour modulation in the NGC 300 galaxy★

A. Sacchi[1,2], P. Esposito[1,3], D. de Martino[4], R. Soria[5,6,7], G. L. Israel[8], A. A. C. Sander[9], L. Sidoli[3], D. A. H. Buckley[10,11,12], I. M. Monageng[10,11], A. Tiengo[1,3], M. Arca Sedda[13,14,9], C. Pinto[15], R. Di Stefano[2], M. Imbrogno[16,8], A. Carleo[17,18], and G. Rivolta[19]

[1] Scuola Universitaria Superiore IUSS Pavia, Palazzo del Broletto, Piazza della Vittoria 15, 27100 Pavia, Italy
e-mail: paolo.esposito@iusspavia.it
[2] Center for Astrophysics|Harvard & Smithsonian, 60 Garden Street, Cambridge, MA 02138, USA
e-mail: andrea.sacchi@cfa.harvard.edu
[3] INAF – Istituto di Astrofisica Spaziale e Fisica Cosmica di Milano, Via A. Corti 12, 20133 Milano, Italy
[4] INAF – Osservatorio Astronomico di Capodimonte, Salita Moiariello 16, 80131 Napoli, Italy
[5] INAF – Osservatorio Astrofisico di Torino, Strada Osservatorio 20, 10025 Pino Torinese, Italy
[6] College of Astronomy and Space Sciences, University of the Chinese Academy of Sciences, Beijing 100049, PR China
[7] Sydney Institute for Astronomy, School of Physics A28, The University of Sydney, Sydney, NSW 2006, Australia
[8] INAF – Osservatorio Astronomico di Roma, Via Frascati 33, 00078 Monteporzio Catone, Italy
[9] Zentrum für Astronomie der Universität Heidelberg, Astronomisches Rechen-Institut, Mönchhofstr. 12-14, 69120 Heidelberg, Germany
[10] South African Astronomical Observatory, PO Box 9, 7935 Observatory, South Africa
[11] Department of Astronomy, University of Cape Town, Private Bag X3, 7701 Rondebosch, South Africa
[12] Department of Physics, University of the Free State, PO Box 339, Bloemfontein 9300, South Africa
[13] Gran Sasso Science Institute (GSSI), Viale Francesco Crispi 7, 67100 L'Aquila, Italy
[14] Physics and Astronomy Department Galileo Galilei, University of Padova, Vicolo dell'Osservatorio 3, 35122 Padova, Italy
[15] INAF – Istituto di Astrofisica Spaziale e Fisica Cosmica di Palermo, Via U. La Malfa 153, 90146 Palermo, Italy
[16] Dipartimento di Fisica, Università degli Studi di Roma "Tor Vergata", Via della Ricerca Scientifica 1, 00133 Roma, Italy
[17] Dipartimento di Fisica "E.R. Caianiello", Università di Salerno and INFN Sezione di Napoli (Gruppo Collegato di Salerno), Via Giovanni Paolo II 132, 84084 Fisciano, Italy
[18] INAF – Osservatorio Astronomico di Cagliari, Via della Scienza 5, 09047 Selargius, Italy
[19] Dipartimento di Fisica "Aldo Pontremoli", Università degli Studi di Milano, Via G. Celoria 16, 20133 Milano, Italy

Received 18 March 2023 / Accepted 23 November 2023

ABSTRACT

We investigate the nature of CXOU J005440.5−374320 (J0054), a peculiar bright (∼4 × 10^{39} erg s^{-1}) and soft X-ray transient in the spiral galaxy NGC 300 with a six-hour periodic flux modulation that was detected in a 2014 *Chandra* observation. Subsequent observations with *Chandra* and *XMM-Newton*, as well as a large observational campaign of NGC 300 and its sources performed with the *Swift Neil Gehrels* Observatory, showed that this source exhibits recurrent flaring activity: four other outbursts were detected across ∼8 years of monitoring. Using data from the *Swift*/UVOT archive and from the *XMM-Newton*/OM and *Gaia* catalogues, we determined that the source is likely associated with a bright blue optical/ultraviolet counterpart. This prompted us to perform follow-up observations with the Southern African Large Telescope in December 2019. With the multi-wavelength information at hand, we discuss several possibilities for the nature of J0054. Although none is able to account for the full range of the observed peculiar features, we found that the two most promising scenarios are a stellar-mass compact object in a binary system with a Wolf–Rayet star companion, or the recurrent tidal stripping of a stellar object trapped in a system with an intermediate-mass (∼1000 $M_\odot$) black hole.

Key words. galaxies: individual: NGC 300 – X-rays: individuals: CXOU J005440.5-374320

1. Introduction

The *Chandra* ACIS Timing Survey at the Brera And Roma astronomical observatories (CATS at BAR) is a systematic search for coherent periodic signals in *Chandra*/ACIS archival data in timed exposure mode. The first catalogue of new pulsators was published in Israel et al. (2016), and several sources have been studied individually (Esposito et al. 2013a,b,c, 2015; Bartlett et al. 2017; Sidoli et al. 2016, 2017). Over 50 new X-ray pulsators have been discovered so far.

CXOU J005440.5–374320 (hereafter J0054) was discovered in the CATS at BAR project with a large-amplitude flux modulation at a period of ∼6 h. It is seen projected in the sky inside the inner region of the NGC 300 (Fig. 1), a face-on spiral galaxy (Scd) in the Sculptor group at a Cepheid distance of 1.88 Mpc (Gieren et al. 2005, corresponding to a distance modulus of 26.4 mag).

NGC 300, due to its proximity and favourable inclination, has been the subject of many studies of its stellar populations (Bresolin et al. 2009, and references therein), star formation history (Butler et al. 2004), Wolf–Rayet (WR) stars and OB associations (Schild et al. 2003; Pietrzyński et al. 2001), planetary nebulae (Peña et al. 2012), variable stars (Pietrzyński et al. 2002;

★ The spectra are available at the CDS via anonymous ftp to cdsarc.cds.unistra.fr (130.79.128.5) or via https://cdsarc.cds.unistra.fr/viz-bin/cat/J/A+A/682/A151

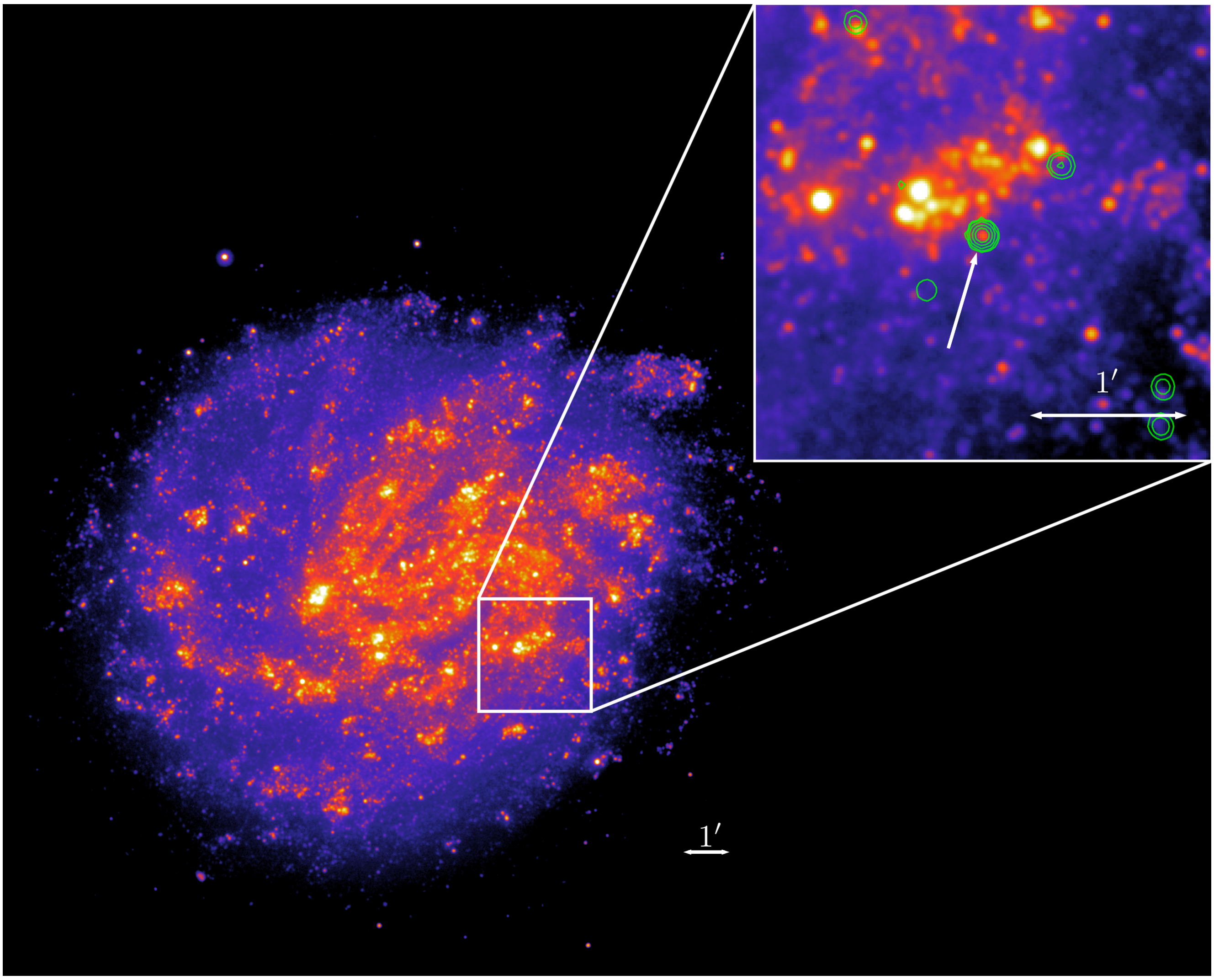

Fig. 1. NGC 300 from *Swift*/UVOT in the UVW2 band. The inset shows the location of J0054, which is indicated by the white arrow. X-ray contours from the *Chandra* detection of November 2014 are plotted in green.

Mennickent et al. 2004), dust content (Helou et al. 2004; Roussel et al. 2005), X-ray sources (Read & Pietsch 2001; Carpano et al. 2005, 2018; Binder et al. 2017; Urquhart et al. 2019), supernova remnants (Blair & Long 1997; Pannuti et al. 2000; Payne et al. 2004; Gross et al. 2019), and UV emission properties (Muñoz-Mateos et al. 2007). NGC 300 has therefore been observed with a wide variety of different telescopes, and a large amount of multi-wavelength data is available.

In this work we focus on the nature of J0054. In Sect. 2 we present the datasets and the observational properties of the source, highlighting its X-ray behaviour and its optical/UV counterpart. In Sect. 3 we discuss possible scenarios for the origin of the J0054 emission, and make our concluding remarks.

2. Observational properties

2.1. X-ray datasets

2.1.1. *Chandra*

J0054 fell into the *Chandra* field of view four times (see Table A.1). The data were reprocessed and reduced with the *Chandra* Interactive Analysis of Observations software package (`CIAO`, v.4.12; Fruscione et al. 2006) and the `CALDB` 4.9.0 release of the calibration files. In the first two visits the source was not detected and 3σ upper limits on its flux were obtained with the `CIAO` tool `srcflux`, following the default Bayesian approach. In the two most recent observations, the source is located at 3.7 and 6 arcmin, respectively, from the telescope aim point. The source counts were extracted from elliptical regions with semi-major and semi-minor axes of 3.2 and 2.6 arcsec for the November 2014 observation, and of 5 and 4 arcsec for the April 2020 observation, corresponding to a point spread function (PSF) fraction of about 96%. Backgrounds were estimated from source-free annular regions, centred on the source position of 10 and 20 arcsec radii.

2.1.2. *Swift*/XRT

Owing to the large monitoring campaign performed on NGC 300 and its sources, the location of J0054 was in the *Swift*/XRT field of view on numerous occasions (170 times by the end of 2022) over more than 15 years, but it was detected in only four visits, August 2018, January 2019, April 2020, and one last time in September 2020, as reported in Table A.1. Count rates and 3σ upper limits for all the observations in which the source was not detected were extracted using the `ximage` tool `sosta`, following the default Poissonian approach. A Bayesian approach was also

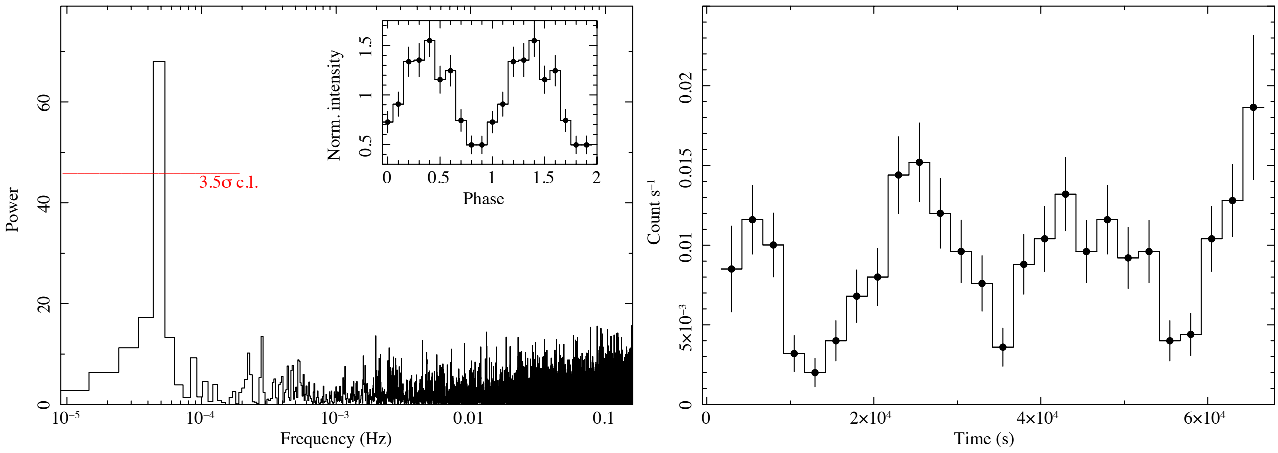

Fig. 2. Timing analysis of J0054. Left panel: Fourier power spectrum of the *Chandra* data of J0054. The red line indicates the local 3.5σ detection threshold adopted in the CAT at BAR project. The prominent peak well above the threshold (5.9σ) corresponds to the ~6 h modulation of J0054. The inset shows the pulse profile obtained by folding the data at the best period of 5.88 ± 0.12 h. Right panel: light curve (the background is negligible). The bin time is 2500 s.

tested, and provided slightly deeper upper limits, yet still compatible with the Poissonian values. Merging all the *Swift*-XRT non-detections, the total exposure time amounts to ≈570 ks, but the source still could not be detected. The 3σ upper limit on the stacked observation is 8.05×10^{-5} cts s^{-1}, corresponding to a flux limit of 2.2×10^{-15} erg cm^{-2} s^{-1} (assuming the best-fitting model described below).

2.1.3. *XMM-Newton*

The position of J0054 was imaged with *XMM-Newton* seven times, as reported in Table A.1, but the source was never detected. For each observation the data were retrieved from the *XMM-Newton* science archive and reduced following the standard procedure. The 3σ upper limits were obtained from the EPIC-pn cameras, with the sole exception of the fourth observation, in which the source falls on EPIC-pn's border, and hence data from the merged EPIC-MOS cameras were used. The merging of the MOS cameras was performed with the sas tool `merge`. The 3σ upper limits were obtained with the `eupper` tool, from a circular region of 15″ radius centred on J0054 position, with background counts extracted from a nearby free-of-sources circular region of 30″ radius on the same detector chip, following the default Bayesian approach.

2.2. Short-term variability

The CATS at BAR pipeline detected the uncatalogued X-ray source J0054 in a ≈60 ks exposure carried out in November 2014 (Table A.1), and singled it out as a new X-ray pulsator with a ~6 h flux modulation (Fig. 2). Taking into account the 16 377 independent trials, the false alarm probability was ~7.6×10^{-11}, which corresponds to a 6.5σ detection. After correcting for the (mild) red noise in the exposure, following Israel & Stella (1996), we evaluated the significance of the signal at 5.9σ. Due to the relatively poor statistics, the approach of using the light curve to estimate the significance of modulation is not recommended because it results in an underestimation of the real statistical level. Nonetheless, as an additional test, we compared the fit of the light curve with a constant and with a constant plus a sinusoidal component. This comparison gives an F-test probability of 5σ that the addition of the sinusoid is significant.

As a further test, we also simulated 10^5 Fourier power spectra with the same properties as that of *Chandra* (Poissonian noise plus an additional $f^{-\alpha}$ component, where $\alpha = 0.71 \pm 0.05$ is inferred by fitting the power spectra distribution continuum of the original *Chandra* dataset), and we verified that no significant peak was detected by the used detection algorithm (which takes into account any additional non-Poissonian noise component) at frequencies shorter than 10^{-3} Hz, setting a probability threshold of 10^{-5} (>4.4σ) at the 5.88 h period frequency. The above numbers are consistent with the 5σ and the 5.9σ level inferred by using two different independent approaches. Correspondingly, we conclude that the signal significance is larger than >4.4σ, and likely lies in the 5–5.9σ range.

From the fit of the sinusoidal function, we derived a period of $P = 5.88 \pm 0.12$ h, which is entirely consistent with that reported in Israel et al. (2016). The pulsed fraction, estimated from the semi-amplitude of the sinusoidal function, was 52 ± 4%. With a $\nu/\Delta\nu$ factor of ~10, the signal is seemingly coherent (i.e., strictly periodic), but this is something difficult to assess when only a few cycles are sampled, and thus a quasi-periodic modulation cannot be excluded.

In the last *Chandra* visit, no significant pulsation was detected, although the 3σ upper limit on the pulsed fraction is about 50%. In the four *Swift*/XRT detections, the signal-to-noise ratio was too low to carry out a meaningful timing analysis.

2.3. Long-term variability

Owing to the long-term monitoring of NGC 300, we were able to trace the J0054 X-ray variability across more than two decades (an early 1990s ROSAT upper limit is unfortunately too shallow to be relevant in this regard). J0054 had never been detected before the *Chandra* pointing of November 2014 (Obs.ID 16029). The closest observation is the non-detection by *Chandra* six months earlier, in May 2014 (Obs.ID 16028). The 3σ upper limit obtained in May 2014 implies a flux variation of at least a factor of 100. After this, J0054 was not pointed for ~1.5 years, and when NGC 300 was observed again, it had disappeared: it is not detected in three short observations by *Swift*/XRT in April 2016 (although the upper limits for these observations are very shallow), nor in two longer observations by *XMM-Newton* at the end of the same year. J0054 reappeared in a *Swift*/XRT observation in late August 2018;

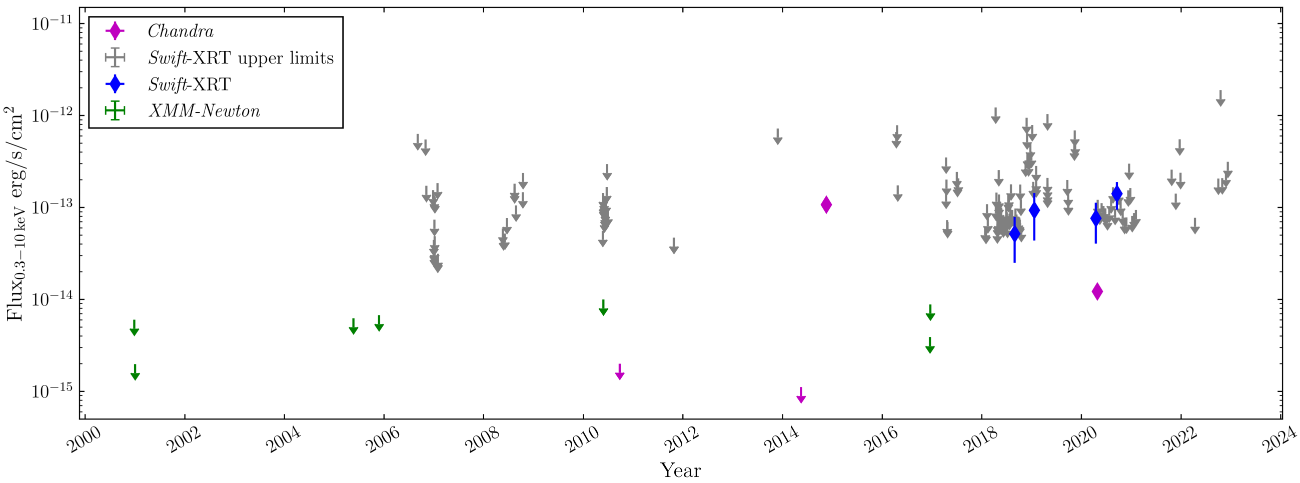

Fig. 3. Long-term X-ray light curve of J0054. The magenta and green data refer to *Chandra* and *XMM-Newton* data, respectively; the down-pointing arrows indicate 3σ upper limits, while the diamond markers indicate detections (with 1σ error bars). *Swift*/XRT detections are shown as blue diamonds, while the upper limits are indicated by down-pointing grey arrows. Count rates for the upper limits and for the *Swift*/XRT detections were converted to fluxes assuming the same spectral shape of the *Chandra* 2014 detection. Years are on the *X*-axis and flux in the 0.3–10 keV band is on the *Y*-axis.

unfortunately, the upper limits around this detection are too shallow to reconstruct the detailed source behaviour. The scene was repeated in January 2019, April 2020, and September 2020. In April 2020 J0054 was detected by both *Swift*/XRT (Obs.ID 00095672001) and *Chandra* (Obs.ID 22375) less than ten days apart. After September 2020, J0054 was never detected again, possibly also due to the visits on NGC 300 growing sparser and shallower with time. Figure 3 shows the long-term light curve of J0054 in the years from approximately 2000–2023; the count-rates were converted into fluxes with the model described below.

2.4. Spectral fitting

Here we address the X-ray spectral fitting of J0054. In particular, we focus on its first detection with *Chandra* in November 2014, which is the dataset with the highest count statistics.

The spectra, the spectral redistribution matrix, and the ancillary response file were generated using the `CIAO` script `specextract`. The spectrum of J0054 was fed into the spectral fitting package `Xspec` (Arnaud 1996) version 12.12.1. Spectral channels having energies below 0.5 keV and above 7.0 keV were ignored in the fit, owing to the very low signal-to-noise ratio from J0054 (essentially all the counts are between approximately 0.7 and 1.7 keV). The spectra were grouped to have a minimum of one count per energy bin, and the *C*-statistic (Cash 1979) was employed (for the spectra shown in Fig. 4, further rebinning was adopted for display purposes only).

We fit a number of different simple models to the spectra, including (but not limited to) the blackbody (BBODY), power-law, bremsstrahlung, Raymond–Smith plasma (Raymond & Smith 1977), hot diffuse gas (MEKAL; Mewe et al. 1985, 1986; Liedahl et al. 1995), collisionally ionized gas (APEC, Smith et al. 2001), and accretion disc models with multi-blackbody components (DISKBB; with standard colour-correction factor fixed at 1.7, Lorenzin & Zampieri 2009); all corrected for interstellar absorption (TBABS; with N_H fixed to the Galactic value 9.45×10^{20} cm^{-2}; HI4PI Collaboration 2016). The abundances used are those of Wilms et al. (2000), with the photoelectric absorption cross-sections from Verner et al. (1996).

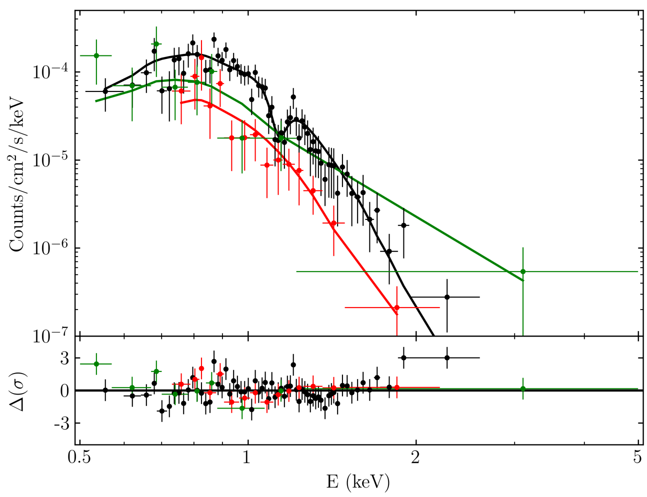

Fig. 4. X-ray spectra of J0054. The upper panel shows the folded spectra and best-fitting model, the lower panel shows the residuals. The data from *Chandra* November 2014, April 2020, and the *Swift*/XRT merged detections are shown as black, red, and green dots, respectively. The solid lines indicate the best-fitting SLIMD model.

While the power-law, MEKAL, APEC, Raymond–Smith plasma, and bremsstrahlung models provided unacceptable fits (C/ν between 2 and 3, C being the value of the statistic and ν the number of degrees of freedom), both BBODY and DISKBB reproduced the spectrum well, and the fits improved when an extra layer of absorption and an absorption Gaussian line at 1.13 ± 0.01 keV with width fixed to 0 and normalization $K = (-1.4 \pm 0.4) \times 10^{-5}$ photons cm^{-2} s^{-1}, were added (EW = 0.077 ± 0.002 keV). The significance of the extra layer of absorption and of the Gaussian line were tested with simulations. In both instances, the `Xspec` routine `simftest`[1] returned a <0.01% probability that the data are consistent with the model without

[1] `simftest` was employed using default parameters and 10 000 iterations; details on the routine can be found at `https://heasarc.gsfc.nasa.gov/xanadu/xspec/manual/node126.html`

Table 1. X-ray spectral fitting parameters.

Model [(1)]	N_H [(2)]	kT	K [(3)]	M_h [(4)]	L_X [(5)]	C/ν [(6)]	g.o.f. [(7)]
BBODY	$0.73^{+0.16}_{-0.13}$	0.109 ± 0.006	$7.0^{+6.6}_{-2.9} \times 10^{-5}$	–	$1.9^{+1.3}_{-0.8}$	80/80	26%
DISKBB	$0.87^{+0.14}_{-0.15}$	$0.117^{+0.009}_{-0.003}$	$2.2^{+3.8}_{-1.3} \times 10^{3}$	1.0	$4.3^{+1.6}_{-1.8}$	79/80	27%
SLIMD	0.9 ± 0.1	–	$0.11^{+0.02}_{-0.01}$	$1.4^{+1.0}_{-0.4}$	$3.6^{+1.5}_{-0.9}$	74/80	21%

Notes. The errors correspond to a statistic variation $\Delta C = 1$. [(1)]The models are reported with their `Xspec` names. [(2)]Intrisic absorption in units of 10^{22} atoms cm^{-2}. [(3)]Normalization of the model, corresponding to $K = L/D^2$ (with L luminosity in units of 10^{39} erg s^{-1} and D distance of the source in units of 10 kpc) for the BBODY model, $K = (R^2/D^2)\cos\theta$ (with the internal radius R in km and θ inclination of the disc, $\theta = 0$ indicating face-on configuration) for the DISKBB model, and $K = \dot{m}/\dot{m}_{\rm Edd}$ for the SLIMD model. [(4)]BH mass in units of $10^3\,M_\odot$. Derived from the model normalization for the DISKBB and as a fitted parameter for the SLIMD model, in both cases under the assumptions of the Schwarzschild metric and $\theta = 45°$. [(5)]Unabsorbed luminosity in units of 10^{39} erg s^{-1} in the 0.3–7 keV band. [(6)]Value of the C-statistic divided by the degrees of freedom. [(7)]Goodness of the fit from Monte Carlo simulations.

the extra component. Furthermore, the statistic improvement of adding the line is $\Delta C = 35.1$ for three degrees of freedom; even accounting for the 'look elsewhere' effect (e.g., Lyons 2008), as the absorption feature does not line up with a specific atomic transition, by correcting the obtained p-value for the dimension of the energy space (i.e., multiplying it for the ratio of the bandwidth to the average resolution: (2 keV–0.5 keV)/0.05 keV $\approx$ 30), the line significance results to be $>3.9\sigma$. For both models, the best-fit parameters are reported in Table 1.

The BBODY and DISKBB models both provided similar temperatures, $kT \approx 110$–120 eV, and similar amounts of intrinsic absorption, $N_H \approx (0.7$–$0.8) \times 10^{22}$ atoms cm^{-2}. The DISKBB model naturally suggests a black hole (BH) as the accretor. From the fit we get an emitting region of ≈9000 km, which corresponds, under the assumption of the Schwarzschild metric and 45° disc inclination, to a mass of about 1000 $M_\odot$. This model also naturally suggests the presence of an accretion disc. Since J0054 is a transient source, to investigate this possibility better, we tried a model designed to reproduce accretion discs around black holes in transient events: SLIMD (Wen et al. 2022). As in the previous cases, we added the two layers of absorption to the SLIMD model (one fixed to the Galactic value, as above, and the other left free to vary) and an absorption Gaussian line at 1.13 keV, and kept the disc inclination and spin fixed at 45° and 0, respectively. We obtained a good fit (Table 1) for a BH with mass $1.4^{+1.0}_{-0.4} \times 10^3\,M_\odot$ and moderate values of accretion rate ($\dot{m} = 0.11^{+0.02}_{-0.01}\,\dot{m}_{\rm Edd}$, where $\dot{m}_{\rm Edd}$ indicates the maximum Eddington accretion rate) and intrinsic absorption $N_H = 0.9^{+0.1}_{-0.1} \times 10^{22}$ cm^{-2}, where errors correspond to a variation in the statistics $\Delta C = 1$ (1σ). We note that both the BH mass and mass accretion rate heavily correlate with the intrinsic absorption, as shown by the contour plots in Fig. 5. The value of unabsorbed X-ray luminosity (between 0.3 and 7 keV) computed with this model and assuming J0054 is located in NGC 300 amounts to 3.6×10^{39} erg s^{-1}, which is in the regime of the ultraluminous X-ray sources (ULXs; e.g., Kaaret et al. 2017; Pinto & Walton 2023).

The value derived for the BH mass is affected not only by statistical uncertainties, but also by systematic ones: we assumed fixed disc inclination and spin, and of course, the estimate is model dependent. Furthermore, the SLIMD model does not support BH masses lighter than 1000 $M_\odot$, thus preventing us from fully exploring the parameter space, as highlighted by Fig. 5. In order to have an idea of these uncertainties, first of all we performed fits with different BH spin and disc inclination values: prograde rotation ($a_\bullet = 0.99$) and edge-on ($\theta = 90°$) provided heavier masses, up to $\sim10^4\,M_\odot$, although the maximally rotating case ($a_\bullet = 0.99$) provided an unacceptable fit ($C/\nu > 3$).

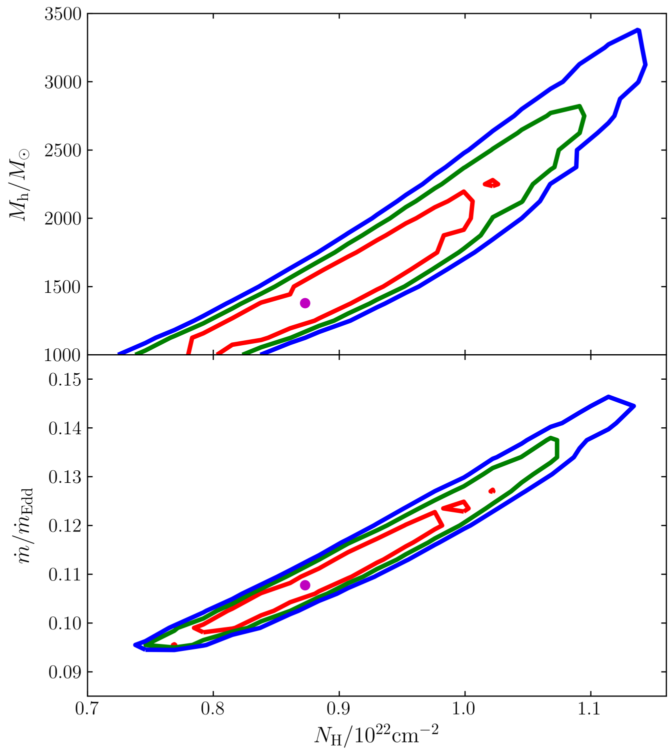

Fig. 5. Contour plots in the BH mass–intrinsic absorption (upper panel) and mass accretion rate–intrinsic absorption spaces (lower panel), obtained with the SLIMD model. The red, green, and blue contours indicate the $\Delta C = 1, 2, 3$ levels, while the magenta dots are the best-fitting parameters.

Counter-rotation ($a_\bullet = -0.99$) and face-on ($\theta = 0°$) configuration provided, instead, lower masses, but the SLIMD model would not allow us to explore the mass regime below 1000 $M_\odot$. To explore the lighter mass regime we employed the SLIMBH model (Sadowski 2011; Straub et al. 2011). This was designed to describe slim accretion discs around Eddington-limited stellar-mass ($\lesssim$100 $M_\odot$) BHs and has an upper limit for the BH mass of 1000 $M_\odot$, thus complementing the SLIMD model. The SLIMBH model with disc inclination fixed at 45° provides an unacceptable fit ($C/\nu > 3$) as the BH mass peaks at 1000 $M_\odot$. A face-on configuration provides an acceptable fit ($C/\nu = 70/85$, 10% goodness of fit, i.e., the percentage of cases, out of 10 000 spectra simulated based on the model, in which the test statistic was less than that of the data) with a BH mass of ≈800 $M_\odot$. Finally, we note that from the DISKBB model, with the corrections by

Lorenzin & Zampieri (2009), the mass can be estimated from 320 to 1000 $M_\odot$ in a 90% range for the inclination (0°–85°). All in all, although we can poorly constrain the BH mass, as it ranges from ∼300 to 10^4 $M_\odot$, the spectral results consistently indicate an IMBH.

Unfortunately, the spectra obtained in the other detections do not afford the possibility to perform meaningful spectroscopic analysis: the latest *Chandra* detection, in April 2020, is heavily affected by the loss of effective area of the ACIS camera below 0.7 keV, while the four *Swift*/XRT detections, taken individually, have a signal-to-noise ratio that is too low for a spectrum to be extracted. Nonetheless, we tentatively merged data from all four *Swift*/XRT detections with the `ftool` routine `extractor` and extracted a merged spectrum with `xselect` from a circular region of 20 arcsec radius centred on the source position. The background was extracted from a free-of-sources circular region of 1 arcmin radius at a 3 arcmin distance from the J0054 location and was likewise merged. In this way we reached a total of 32 net counts with a source fraction of the total counts evaluated at 94.3%. We then fitted the best-fitting model we obtained above simultaneously to the three spectra (*Chandra* from November 2014 and April 2020, and *Swift*/XRT from the combined datasets). We froze all parameters to the best-fit values, except for the normalizations (for the SLIMD model, this corresponds to the mass accretion rate). We obtained an acceptable value of the statistic (C = 119 with 145 degrees of freedom and goodness of 31%) with no Gaussian lines in the latest *Chandra* observation and in the merged *Swift*/XRT spectra and mass accretion rates equal to 0.07 and 0.09 $\dot{m}_{\rm Edd}$, respectively. We can conclude that the emission of J0054 in the latest *Chandra* and in the *Swift*/XRT detections is compatible with that observed in the first *Chandra* detection, although spectral evolution or variations in the amount of intrinsic absorption cannot be assessed. Figure 4 shows the three spectra and their residuals, as well as the best-fitting model.

2.5. Optical/UV counterpart

2.5.1. UVOT photometry

As the location of J0054 was visited several times with *Swift*, we possess a large number of *Swift*/UVOT observations, which cover each of the six UVOT optical/UV bands: V (5468 Å), B (4392 Å), U (3465 Å), UVW1 (2600 Å), UVM2 (2246 Å), and UVW2 (1928 Å). Based on visual inspection, we removed any observations in which a smoke-ring feature, generated by the nearby foreground G8 star CD-38 301 (Cruzalèbes et al. 2019), was superimposed at the J0054 location.

We found no trace of significant variability (within 1σ, roughly corresponding to half a magnitude) in any of the six bands; in particular, we found none in coincidence with the X-ray flaring activity, as shown in Fig. 6, which highlights the difference between the UVW2 AB magnitude and the 0.3–10 keV flux at the epoch of the latest flare. As no variability was detected, all observations were stacked using the `ftool` routine `uvotimsum` and fluxes were extracted using `uvotsource` (with flag APERCORR = curveofgrowth) from a circular region centred on the source position and with a radius of 5 arcsec. Backgrounds were estimated from a circular region of 10 arcsec radius, free of sources, at approximately 15 arcsec from the source location. The AB magnitudes from the merged *Swift*/UVOT observations, as well as the averaged magnitudes over the single observations, are reported in Table 2.

In order to correct the *Swift*/UVOT spectral energy distribution (SED) for dust extinction we adopted different strategies.

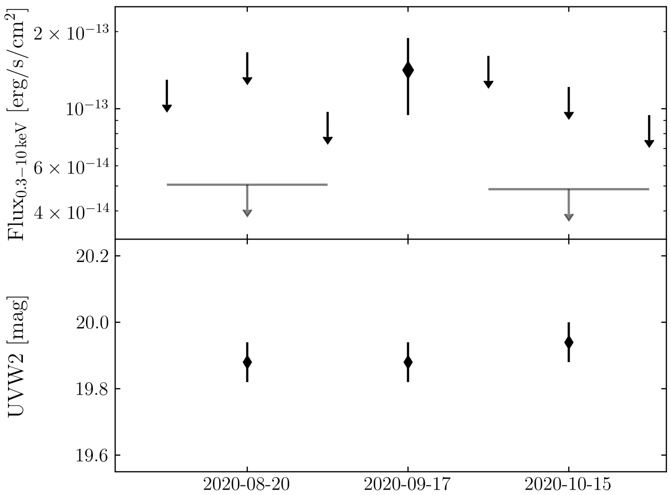

Fig. 6. X-ray flux (upper panel) and UVW2 AB magnitude (lower panel) evolution during the flare detected in the September 2020 *Swift* data. The X-ray upper limits in the single observations are reported as black arrows; the upper limits derived from the merged observations are reported as grey arrows. UVW2 magnitudes for each of the three epochs were derived by merging the single orbit exposures.

The minimum possible value of the reddening is the Galactic line-of-sight value $E(B-V)$ = 0.0108 (Schlafly & Finkbeiner 2011): in this case, the optical/UV SED would be consistent with a blackbody profile of ≈15 000 K and a luminosity of 7.5 × 10^4 $L_\odot$, compatible with a blue supergiant star ($M_V \approx -6.5$ mag). A slightly higher reddening was adopted by Gieren et al. (2004), who assumed a foreground Galactic $E(B-V)$ = 0.025 mag (Burstein & Heiles 1984) plus a reddening $E(B-V)$ = 0.05 mag through the halo of NGC 300. In this case, the best-fitting blackbody temperature rises to about 17 000 K and the luminosity to 10^5 $L_\odot$, still compatible with a single blue supergiant star ($M_V \approx -6.7$ mag). However, the complete absence of individual stellar lines in the observed optical spectra (see Sect. 2.5.3) makes it unlikely that the observed SED stems from a barely reddened, single blue supergiant or a (very) late-type WR star with a comparable temperature (e.g., Sander et al. 2014).

The other extreme in terms of possible extinction would be to use the $N_{\rm H}$ inferred from the X-ray spectral modelling. Converted to an optical extinction A_V via the empirical relation in Foight et al. (2016), this would imply $A_V \approx 3.1$ mag, and hence an absolute brightness $M_V \approx -9.6$ mag. Such a source would be too luminous to be a single star and would further be unphysically blue ($B-V \approx -1.2$ mag) for any star, cluster, or blackbody-like spectrum. Thus, we can rule out such a high extinction for the optical counterpart. Assuming a physically meaningful limit of $B-V \gtrsim -0.5$ mag and $U-B \gtrsim -1.5$ mag, we can place an upper limit on the total extinction of $A_V \lesssim 1$ mag. In this case the photometry is compatible with a young stellar cluster (YSC) with an age of ≲4 Myr and ≈10^3 $M_\odot$, assuming instantaneous star formation and a Large Magellanic Cloud (LMC)-like metallicity (similar to that of NGC 300; Gazak et al. 2015; Toribio san Cipriano et al. 2016). This would correspond to a small stellar population dominated by three or four main-sequence O stars and about 12–15 B stars (see Sect. 2.5.3).

2.5.2. Archival data

J0054 is also present in the *XMM-Newton*/OM catalogue of serendipitous sources (Page et al. 2012). Our source location

Table 2. UV/optical magnitudes from *Swift*/UVOT and *XMM-Newton*/OM.

Instrument	Epoch	AB magnitude					
		V	*B*	*U*	UVW1	UVM2	UVW2
Swift/UVOT (merged)	–	19.84 ± 0.09	19.66 ± 0.05	19.75 ± 0.03	19.93 ± 0.04	20.06 ± 0.05	20.16 ± 0.05
Swift/UVOT (averaged)	–	19.82 ± 0.11	19.56 ± 0.09	19.77 ± 0.07	19.79 ± 0.07	19.85 ± 0.06	19.92 ± 0.05
XMM-Newton/OM	2000-12-26	–	20.2 ± 0.1	–	–	–	–
	2001-01-01	–	20.1 ± 0.1	20.3 ± 0.1	19.5 ± 0.1	–	–
	2005-05-22	–	–	20.0 ± 0.1	19.9 ± 0.1	20.2 ± 0.1	–
	2005-11-25	–	–	20.0 ± 0.1	19.62 ± 0.05	20.1 ± 0.1	–
	2016-12-17	–	–	–	–	20.3 ± 0.1	–
	2016-12-19	–	–	–	–	20.1 ± 0.1	–

Notes. *Swift*/UVOT AB magnitudes from the merged observations and averaged over the single observations. *XMM-Newton*/OM magnitudes are from the *XMM-Newton*/OM catalogue (Page et al. 2012). U and UVW1 magnitudes from the 2016 *XMM-Newton*/OM observations have not been reported as they are affected by the 'smoke ring' feature. Quantities are reported with 1σ errors.

was visited six times, as reported in Table 2. *XMM-Newton*/OM data are compatible with the *Swift*/UVOT data when one considers that, at the magnitudes of our source, discrepancies as large as 1 mag are not uncommon between *Swift*/UVOT and *XMM-Newton*/OM (see Yershov 2014 and the *XMM-Newton*/OM calibration report[2]). J0054 is also present in the *Gaia* catalogue (Gaia Collaboration 2023), with a parallax $p = 0.53 \pm 0.78$ mas, corresponding to a distance of $1.2^{+0.5}_{-0.4}$ kpc (Lindegren et al. 2021; Bailer-Jones et al. 2021). However, at a magnitude $G = 20.49$ ($G_{\rm BP} = 20.61$ and $G_{\rm RP} = 20.37$), the source is rather faint for *Gaia* and the low signal-to-noise ratio parallax is probably unreliable.

2.5.3. SALT spectrum

Two spectra were acquired on December 2 and December 15, 2019 (Progr.ID: 2018-2-LSP-001), with the Southern African Large Telescope (SALT; Buckley et al. 2006; O'Donoghue et al. 2006), equipped with the Robert Stobie Spectrograph (RSS) (Burgh et al. 2003; Kobulnicky et al. 2003) in the long-slit (8′ × 1″.5) spectroscopy mode. The PG0300 and PG0900 gratings were used for the observations with exposure times of 1800 s and 2000 s, respectively. A grating tilt of 5°.4 was used for the PG0300 observation, which covered the wavelength range 3700–7500 Å and provided a resolving power of 250–600. For the PG0900 observation, a tilt of 15°.125 (4200–7250 Å) was used, with a resultant resolving power of 800–1200. The position angle (PA) was 0 deg from north and the average seeing during the observations was 1″.5.

Standard spectral reduction (bias, flat-field, sky subtraction, and cosmic-ray removal) was performed using the PySALT pipeline (Crawford et al. 2010). The wavelength calibration was performed with Ar (PG0300) and Xe (PG0900) lamps, and the 1D spectrum was extracted using various tasks in IRAF. Since no spectrophotometric standard star was observed, the spectra are not calibrated in flux.

The two spectra show similar features and display strong emission lines of Balmer series and neutral He, as well as forbidden lines of [OII], [OIII], [NeIII], [NII], and [SII], with a blueward asymmetry, probably due to composite components in the emitting region, which however cannot be resolved with this resolution (see Fig. 7; the lower-resolution spectrum is shown in Fig. B.1 and the parameters of the main lines, which were derived from Gaussian fits, are given in Table B.1).

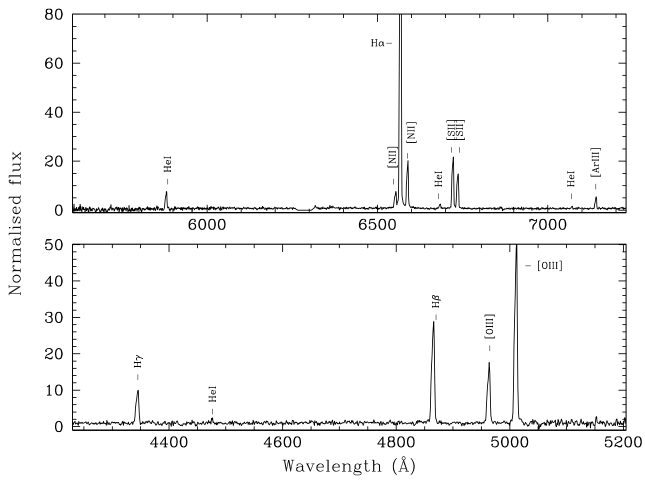

Fig. 7. SALT spectrum (PG0900) of J0054.

The lack of flux calibration does not allow us to measure emission line flux ratios. However, we can use the broad-band SED from *Swift*/UVOT and the unabsorbed blackbody fit described in Sect. 2.5.1, to estimate an approximate continuum flux level (assuming that it did not change substantially between the *Swift* and SALT observations), and then convert the measured line equivalent width (EW) to line fluxes. In particular, we used the P0900 grating spectrum from December 15, 2019, which provides the more reliable measurement of the line profiles because of its higher resolution.

We find an observed flux ratio $F(H_\alpha)/F(H_\beta) \approx 2.9$ and $F(H_\gamma)/F(H_\beta) \approx 0.47$, perfectly consistent with photo-ionized gas in HII regions (Case B recombination) without any reddening corrections apart from the line-of-sight Galactic component. Our simulations with the STARBURST99 code (Leitherer et al. 1999, 2014) show that the EWs of H_α and H_β are consistent with those expected from photo-ionized gas illuminated by a YSC with the same continuum flux we observed. Both of those findings suggest that the emission lines are from an extended ionized nebula rather than from the direct stellar counterpart of the X-ray source. Moreover, the ionized gas sees the same continuum flux as we observe. If there is additional intrinsic extinction, it must be located between the X-ray source and the surrounding nebula, rather than between the source of the line emission and the

[2] https://www.cosmos.esa.int/documents/332006/2169043/calibration_om.pdf

line-of-sight. We note that an O-type ionizing star embedded in a HII region is not supported by the lack of absorption features of HeII and HeI (McLeod et al. 2015, 2020), while only HeI in emission is observed.

If the 6 h periodicity identified in the X-ray light curve corresponds to the orbital period of a binary system, a compact WR-like donor is needed; assuming a total mass of the system of $\approx 30\,M_{\odot}$ and a mass ratio of ≈ 3, the binary separation amounts to $\approx 5\,R_{\odot}$ and the upper limit on the radius of the companion to $\approx 2.5\,R_{\odot}$. However, our SALT spectra do not show any explicit WR features, such as broad HeII 4686 Å emission (e.g., Dodorico et al. 1983). In addition, the lack of a number of diagnostic lines (Schild & Testor 1992) does not support a WC or a WN: CIII, CII, or CIV for the former and NIII 4100 Å and 4640 Å for the latter are not detected. While this could in principle be explained by a compact ('stripped') star that does not show WR-type spectral features (e.g., Götberg et al. 2018), such stars are a huge source of HeII ionizing flux (e.g., Sander & Vink 2020; Sander et al. 2023), which should result in nebular HeII emission, which is absent as well. We thus ran STARBURST99 simulations to test whether stellar line emission features from a WR star could be hidden in a YSC with the observed continuum brightness and the line emission from its surrounding HII region. Assuming the same uniform extinction $A_V \approx 1$ mag for both the YSC and a WR star inside it, we verified that all features of a typical compact WR star would be sufficiently diluted at least for some classes of WR stars. For the WR star we used LMC models from Hainich et al. (2014) calculated with the PoWR (Gräfener et al. 2002; Hamann & Gräfener 2003; Sander et al. 2015) model atmosphere code and diluted to the distance of NGC 300. From our calculations we can thus conclude that the lack of observed WR emission lines in the SALT spectra does not rule out the scenario of a WR donor for the X-ray source. Moreover, an additional viable scenario is that the extinction around the X-ray binary system (including a WR donor with a dense wind) is higher than the extinction of the surrounding group of OB stars, which would further dilute or completely hide strong WR emission lines.

3. Discussion

J0054 is a puzzling source. It was discovered as a bright X-ray pulsator with a 6 h modulation; it shows a peculiar supersoft X-ray spectrum, and also displayed long-term variability. The available spectroscopy and photometry for the optical/UV counterpart show no hints of variability, but reveal only an HII region. While the photometry as such could match an individual B star the strong absorption in the X-ray regime indicates that the photometry reflects an unresolved population of stars. Thus, any B star, O star, WR star, or even a whole YSC are viable options. In any case, the optical/UV and X-ray cannot be fitted simultaneously by a single blackbody or disc model, nor is it possible to intercept the optical/UV data extrapolating the model best-fitting the X-ray and vice versa (even accounting for the parameters' uncertainties), as clearly demonstrated by Fig. 8, which shows the full SED and the absorbed and de-absorbed models. This suggests that the two emissions, optical/UV and X-ray, have different origins. Here we discuss different scenarios that could explain its peculiar multi-wavelength appearance.

Projected in the sky, J0054 is seen well inside the $B - R_{25}$ radius[3] of NGC 300, at only 3.4 arcmin (about 1.9 kpc) from the centre of the galaxy. In addition, the Galactic latitude is $b \simeq -79.^{\circ}4$, making a Galactic foreground object highly unlikely. The only piece of information that possibly suggests a foreground Galactic object is the *Gaia* parallax, which is, however, probably unreliable given its low S/N. In the hypothesis of a Galactic object, in view of the 6 h modulation, the pulse profile, and the flux, a cataclysmic variable (CV) is the only plausible candidate (although the X-ray spectrum discourages this interpretation and CVs are very unlikely to occur at the latitude of J0054; e.g., Drake et al. 2014). If the X-ray period traces the binary motion, for a CV in a 6 h orbit, a donor of spectral type of K7V (Knigge 2006) is expected. If we assume for it $M_V = 7.7$, $B - V = 1.3$, and $V - R = 1.15$ (e.g., Johnson 1966; Gray & Corbally 2009), the possibility appears unlikely, since a late-type K7V would be too bright and red with respect to our source optical counterpart. In the case of weakly magnetic or non-magnetic system, the relationship between luminosity and orbital period by Warner (1987) indicates absolute magnitudes of $V \approx 4$ in a high state or ≈ 8 while in quiescence. In general, the absolute magnitudes of such systems are always between 8 and 2 (Ramsay et al. 2017), and are therefore incompatible with the optical counterpart of J0054.

The lack of correlation between the X-ray flares and the optical/UV emission and the overall lack of significant variability at optical/UV wavelengths across years does not support a nova at later stages (Williams et al. 1994; Williams 2016) nor a supersoft source (SSS; van den Heuvel et al. 1992). A SSS scenario, on the other hand, is also discouraged by the fact that the observed X-ray and optical luminosity would require a massive WD, of about $1.2\,M_{\odot}$ (Starrfield et al. 2004) and this would place J0054 at $\approx$50–200 kpc, which would result in an isolated intergalactic SSS, a highly unluckily occurrence.

The most natural way to explain the multi-wavelength behaviour of J0054 is probably an ultraluminous supersoft X-ray source (ULSs) scenario. ULSs can be considered as high-inclination, high-accretion-rate compact objects. Here the

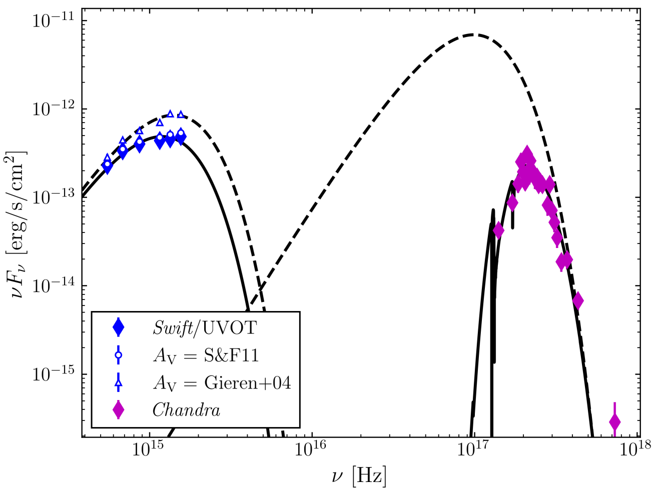

Fig. 8. Full SED of J0054. The magenta and blue diamonds show the *Chandra* and *Swift*/UVOT data, respectively. The black solid lines show the two independent best-fitting models for the two components with no absorption correction, and the dashed black lines show the de-absorbed models. For *Swift*/UVOT, the full markers indicate the observed flux, while the empty blue markers the de-absorbed fluxes, corrected following the different values discussed in the text (the full markers lie under the empty ones). For *Chandra*, the de-absorbed model was obtained by setting to 0 the amount of N_H.

[3] The 25th magnitude isophote in the blue B band (de Vaucouleurs et al. 1991).

hard X-ray photons coming from the inner regions are significantly blocked by a strong optically thick wind, which manifests itself in the form of Doppler-shifted absorption lines similar to the feature shown at 1.13 keV in Fig. 4 (Pinto & Walton 2023; Urquhart & Soria 2016). Moreover, this feature seems to be a hallmark strongly associated with the ULS population (Urquhart & Soria 2016).

A well-known example is NGC 247 ULS or X-1 for which high-resolution spectra resolved the 1 keV feature into a forest of lines produced by a powerful 0.17c wind (Pinto et al. 2021); this source also exhibits modulations on timescales of a few ks (Alston et al. 2021). Here, the spectral-timing analysis would rather support the case for a heavy NS or a small stellar-mass BH accreting well beyond the Eddington limit (D'Aì et al. 2021).

J0054 also shares some spectral characteristics of M 101 ULX-1, a well-studied ULX and SSS consisting of a stellar-mass BH and a WR star (Liu et al. 2013). The only object compatible with the 6 h modulation, if it reflects the binary orbit, is a WR star (see Esposito et al. 2013a, 2015; Qiu et al. 2019 for the discussion of similar systems and candidates). As discussed in Sect. 2.5.3, a WR star, isolated or belonging to a YSC, is not excluded by the optical information. For the compact object it is unsafe to rule out a neutron star only on the basis of the observed super-Eddington luminosity (e.g., Bachetti et al. 2014; Israel et al. 2017); however, a stellar-mass BH is the most likely compact object in WR binaries for evolutionary reasons (van den Heuvel et al. 2017). The two sources exhibit a highly variable (by a factor of ≈300) X-ray emission with a similar spectrum (at least in some states of M 101 ULX-1), in particular, similar temperatures and sizes, and a dip at 1.1 keV (Soria & Kong 2016; Urquhart & Soria 2016).

Finally, it is worth mentioning that the NGC 300 galaxy hosts another bright source, NGC 300 X-1, which hosts a WR star feeding a massive black hole candidate (with a dynamically inferred mass of $20 \pm 4\,M_\odot$, although a lighter compact object cannot be completely ruled out; Laycock et al. 2015) which sometimes crosses the 10^{39} erg s^{-1} threshold (Crowther et al. 2010; Earnshaw & Roberts 2017).

The fact that the absorption inferred from the X-ray spectrum is local to the X-ray source and does not involve the optical counterpart (as demonstrated in Sect. 2.5.1) might support an outflowing wind in this scenario. However, the main problem with a ULX/ULS scenario is probably the transient nature of the source; with a compact object in such a tight orbit with a strongly winded WR star, one would always expect significant accretion. A possible solution to this would be interpreting the variability in terms of obscuration, which would likely result in spectral changes. The available data, unfortunately, are inconclusive about this matter. Finally, we note that this source is not present in any ULX/ULS catalogues (e.g., Walton et al. 2022): although its unabsorbed luminosity exceeds the 10^{39} erg s^{-1} threshold, its observed absorbed luminosity does not.

A radically different scenario that is capable of explaining some of the features of J0054 is the partial tidal disruption of a star by an intermediate-mass BH (IMBH). Tidal disruption events (TDEs) usually occur when a star wanders too close to a supermassive BH (SMBH), and its binding self-gravity is overcome by the BH's tidal forces, which tear the star apart. Part of the stellar debris is subsequently circularized and accreted, emitting a bright electromagnetic (EM) signal, and part gets ejected (Rees 1988; Phinney 1989). TDEs, although they are bright across the whole EM spectrum, from radio to γ rays (e.g., Swift J1644, Burrows et al. 2011), in the X-ray band they usually appear as luminous supersoft transients. The X-ray spectrum

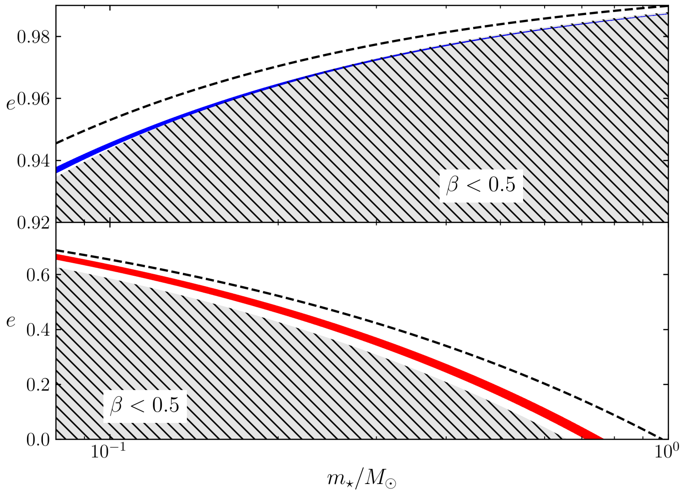

Fig. 9. Orbital eccentricities and stellar mass values compatible with the BH mass and mass accretion rate obtained from the spectral fitting. The blue and red regions indicate WD and MS star cases, respectively. The width of the contours covers the 5σ regions. The barred portions of the parameter space are forbidden as they represent the regions where $\beta < 0.5$ (no disruption occurs) and the dashed lines indicate the values for which $\beta = 0.6$.

suggests that the J0054 emission is linked to accretion processes, and the SLIMD model (specifically developed to fit slim disc emission from the tidal disruption of stellar objects by SMBHs) provides an estimate for the mass of J0054 (≈1400 $M_\odot$) and places it in the IMBH class. The TDE hypothesis could also explain the observed long-term X-ray variability. As invoked for XMMU J122939.7+075333 (Tiengo et al. 2022), an object sharing many characteristics with J0054 (long-term variability, very soft X-ray emission, forbidden lines in the optical counterpart), a star on a highly eccentric orbit would be stripped of its material at every pericentre passage, thus producing recurrent flares.

Assuming we spotted the TDE close to its peak luminosity, we can use the mass accretion rate and BH mass obtained from the spectral fit to derive the penetration factor, orbital eccentricity, and mass of the stripped star. To this end, we employed reasonable mass–radius relations for a white dwarf (WD) and for a main sequence star (MS)[4], coupled with the analytical formulas derived by Guillochon & Ramirez-Ruiz (2013) for the $\gamma = 5/3$ polytrope case. Figure 9 shows the possible combination of star mass and orbital eccentricity compatible with the spectral estimates of mass accretion rate and BH mass. The blue and red contours represent the results obtained for a main sequence star and a white dwarf, respectively. The width of the contours corresponds to the 5σ region. The penetration factor β, defined as the ratio between pericentre distance and tidal radius, measures how deep the star dives into the potential well of the hole. As the tidal radius $r_t \simeq r_\star (M_h/m_\star)^{1/3}$ represents the distance at which the BH tidal forces balance the stellar self-gravity, for penetration factors $\beta < 1$ the disruption is only partial. For values of $\beta \lesssim 0.5$ the mass loss of the star stops (Guillochon & Ramirez-Ruiz 2013): in Fig. 9 the grey bars cover these forbidden regions. As Fig. 9 shows, only stars with masses below one solar mass are compatible with the spectral fitting results. Furthermore, for a WD only highly eccentric orbits are permitted, with $0.94 \lesssim e \lesssim 0.96$, while for MS stars only values of eccentricities $\lesssim 0.7$ are

[4] We assumed the relations $r_{MS}/R_\odot = (m_{MS}/M_\odot)^{0.8}$ and $r_{WD}/R_\odot = 0.01(m_{WD}/M_\odot)^{-1/3}$ for a MS donor and a WD donor, respectively.

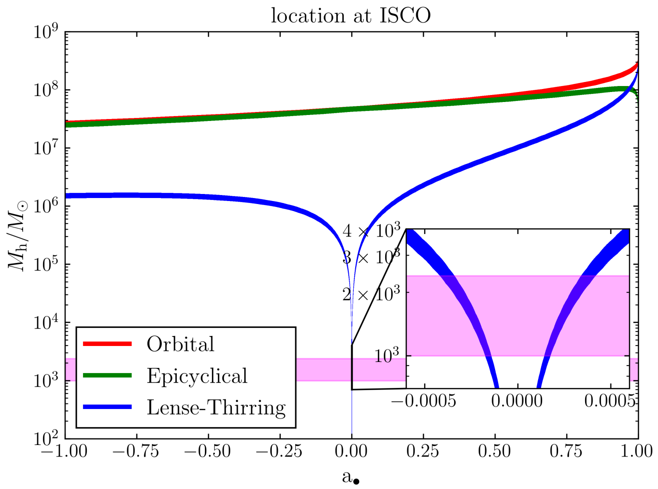

Fig. 10. Contour plot in the BH mass-spin space of the three fundamental frequencies at ISCO for a 47 µHz frequency. The shaded region indicates the BH mass range obtained from the spectral fit. The width of the lines reflects a 5σ range.

permitted. In any case, for both WDs and MS stars, the passage around the BH is shallow: the dashed black line in Fig. 9 represents the values for which the penetration factor is $\beta = 0.6$. As for the case of XMMU J122939.7+075333, the amount of mass accreted at every passage is very small, about $5.5 \times 10^{-10}\, M_\odot$. As pointed out by Tiengo et al. (2022), with these low values of mass getting accreted per passage, one such event can last for very long times, and XMMU J122939.7+075333 has indeed been active for more than two decades. Finally, although the available observations are sparse and often provide only shallow upper limits, the outbursts of J0054 seem to recur on a timescale of ≈5 months, which is the time interval between the two closest outbursts and cannot be ruled out by non-detections.

The TDE scenario could also explain J0054 short-term variability: the observed periodicity could be linked to disc instability in a similar way to that described by Pasham et al. (2019) for the 'text-book TDE' ASASSN-14li (Miller et al. 2015). To investigate this possibility, we can study the fundamental frequencies at the innermost stable circular orbit (ISCO) around the BH. There are three: the Keplerian orbital frequency ν_ϕ, the vertical epicyclic frequency ν_θ, and the Lense–Thirring frequency, given by the beating between these two, $\nu_{\rm LT} = \nu_\phi - \nu_\theta$. Analytical expressions for these frequencies were derived by Kato (1990):

$$\nu_\phi = \frac{c^3}{2\pi G M_{\rm h}}\left[\frac{1}{R_{\rm ISCO}^{3/2} + a_\bullet}\right], \quad (1)$$

$$\nu_\theta = \nu_\phi\left[1 - \frac{4a_\bullet}{R_{\rm ISCO}^{3/2}} + \frac{3a_\bullet^2}{R_{\rm ISCO}^2}\right]^{1/2}. \quad (2)$$

Figure 10 shows the contours, in the BH mass-spin space, for the three described frequencies: Keplerian (in red), vertical epicyclic (in green), and Lense–Thirring (in blue) for a 47 ± 1 µHz frequency (the 5.88 ± 0.12 h modulation). The width of the contours represents the 5σ region. The shaded region shows the BH mass range identified by the spectral fit; its width corresponds to a $\Delta C = 1$. The only frequency compatible with the mass range identified by the spectral fitting is the Lense–Thirring frequency, and only for a non-spinning BH: $|a_\bullet| \lesssim 4 \times 10^{-4}$.

The TDE scenario cannot account for every aspect of J0054. The absorption feature in the X-ray spectrum, around 1 keV is similar to those often observed in SSSs, both Galactic (nuclear burning WD, see e.g., Ebisawa et al. 2001) and extragalactic (ULXs, see e.g., Pinto et al. 2021); however, this feature is usually detected in sources with thick outflows rather than simple disc emission, and only at high values of mass accretion rates. Another weak point in this scenario is the involvement of a non-spinning $10^3\, M_\odot$ IMBH. Although it has been shown that young dense clusters can nurture the seeding of IMBHs (Arca Sedda et al. 2021, and in prep.; Di Carlo et al. 2021; Rizzuto et al. 2021, 2022; Gonzalez et al. 2023), it seems hard for YSCs to grow IMBHs above 1000 $M_\odot$, unless the host YSC has a large central density (e.g., Maliszewski et al. 2022) and the tightly constrained null value of the spin would require some fine tuning for the model to work. On the other hand, the TDE scenario can provide a satisfactory explanation for the X-ray spectral shape, and both the long- and short-term behaviour of J0054.

Acknowledgements. We thank the anonymous referee for the insightful comments and constructive report. This research is based on data and software provided by the NASA/GSFC's High Energy Astrophysics Science Archive Research Center (HEASARC), the *Chandra* X-ray Center (CXC, operated for NASA by SAO), the ESA's *XMM-Newton* Science Archive (XSA), and on observations made with the Southern African Large Telescope (SALT) through the transient followup program 2018-2-LSP-001 (PI:DAHB). A.S., P.E., G.L.I., A.T., and C.P. acknowledge financial support from the Italian Ministry for University and Research, through the grants 2017LJ39LM (UNIAM) and 2022Y2T94C (SEAWIND). D.d.M. acknowledges financial support from INAF Mainstreams and AstroFund 2022 FANS projects grants. R.S. acknowledges grant number 12073029 from the National Natural Science Foundation of China (NSFC). M.I. is supported by the AASS PhD joint research program between the University of Rome "Sapienza" and the University of Rome "Tor Vergata", with the collaboration of the National Institute of Astrophysics (INAF). I.M.M. and D.A.H.B. are supported by the South African NRF. A.A.C.S. is supported by the German Deutsche Forschungsgemeinschaft, DFG in the form of an Emmy Noether Research Group – Project-ID 445674056 (SA4064/1-1, PI Sander). A.A.C.S. further acknowledges support from the Federal Ministry of Education and Research (BMBF) and the Baden-Württemberg Ministry of Science as part of the Excellence Strategy of the German Federal and State Governments. M.A.S. acknowledges funding from the European Union's Horizon 2020 research and innovation programme under the Marie Skłodowska-Curie grant agreement No. 101025436 (project GRACE-BH, PI: Manuel Arca Sedda). P.E. and A.S. thank M. Mapelli, L. Zampieri and G. Lodato for interesting and insightful discussion.

References

Alston, W. N., Pinto, C., Barret, D., et al. 2021, MNRAS, 505, 3722
Arca Sedda, M., Amaro Seoane, P., & Chen, X. 2021, A&A, 652, A54
Arnaud, K. A. 1996, in Astronomical Data Analysis Software and Systems V, eds. G. H. Jacoby, & J. Barnes (San Francisco: ASP), ASP Conf. Ser., 101, 17
Bachetti, M., Harrison, F. A., Walton, D. J., et al. 2014, Nature, 514, 202
Bailer-Jones, C. A. L., Rybizki, J., Fouesneau, M., Demleitner, M., & Andrae, R. 2021, AJ, 161, 147
Bartlett, E. S., Coe, M. J., Israel, G. L., et al. 2017, MNRAS, 466, 4659
Binder, B., Gross, J., Williams, B. F., et al. 2017, ApJ, 834, 128
Blair, W. P., & Long, K. S. 1997, ApJS, 108, 261
Bresolin, F., Gieren, W., Kudritzki, R.-P., et al. 2009, ApJ, 700, 309
Buckley, D. A. H., Swart, G. P., & Meiring, J. G. 2006, in Ground-based and Airborne Telescopes, ed. L. M. Stepp (Bellingham: SPIE), SPIE Conf. Ser., 6267, 62670Z
Burgh, E. B., Nordsieck, K. H., Kobulnicky, H. A., et al. 2003, in Instrument Design and Performance for Optical/Infrared Ground-based Telescopes, eds. M. Iye, & A. F. M. Moorwood, SPIE Conf. Ser., 4841, 1463
Burrows, D. N., Kennea, J. A., Ghisellini, G., et al. 2011, Nature, 476, 421
Burstein, D., & Heiles, C. 1984, ApJS, 54, 33
Butler, D. J., Martínez-Delgado, D., & Brandner, W. 2004, AJ, 127, 1472
Carpano, S., Wilms, J., Schirmer, M., & Kendziorra, E. 2005, A&A, 443, 103
Carpano, S., Haberl, F., Maitra, C., & Vasilopoulos, G. 2018, MNRAS, 476, L45
Cash, W. 1979, ApJ, 228, 939
Crawford, S. M., Still, M., Schellart, P., et al. 2010, in Observatory Operations: Strategies, Processes, and Systems III, eds. D. R. Silva, A. B. Peck, & B. T. Soifer, SPIE Conf. Ser., 7737, 773725

Crowther, P. A., Barnard, R., Carpano, S., et al. 2010, MNRAS, 403, L41
Cruzalèbes, P., Petrov, R. G., Robbe-Dubois, S., et al. 2019, MNRAS, 490, 3158
D'Aì, A., Pinto, C., Del Santo, M., et al. 2021, MNRAS, 507, 5567
de Vaucouleurs, G., de Vaucouleurs, A., Corwin, H. G., Jr, et al. 1991, Third Reference Catalogue of Bright Galaxies (New York: Springer)
Di Carlo, U. N., Mapelli, M., Pasquato, M., et al. 2021, MNRAS, 507, 5132
Dodorico, S., Rosa, M., & Wampler, E. J. 1983, A&AS, 53, 97
Drake, A. J., Gänsicke, B. T., Djorgovski, S. G., et al. 2014, MNRAS, 441, 1186
Earnshaw, H. M., & Roberts, T. P. 2017, MNRAS, 467, 2690
Ebisawa, K., Mukai, K., Kotani, T., et al. 2001, ApJ, 550, 1007
Esposito, P., Israel, G. L., Sidoli, L., et al. 2013a, MNRAS, 436, 3380
Esposito, P., Israel, G. L., Sidoli, L., et al. 2013b, MNRAS, 433, 2028
Esposito, P., Israel, G. L., Sidoli, L., et al. 2013c, MNRAS, 433, 3464
Esposito, P., Israel, G. L., Milisavljevic, D., et al. 2015, MNRAS, 452, 1112
Foight, D. R., Güver, T., Özel, F., & Slane, P. O. 2016, ApJ, 826, 66
Fruscione, A., McDowell, J. C., Allen, G. E., et al. 2006, in Observatory Operations: Strategies, Processes, and Systems, eds. D. R. Silva, & R. E. Doxsey (Bellingham: SPIE), SPIE Conf. Ser., 6270, 62701V
Gaia Collaboration (Vallenari, A., et al.) 2023, A&A, 674, A1
Gazak, J. Z., Kudritzki, R., Evans, C., et al. 2015, ApJ, 805, 182
Gieren, W., Pietrzyński, G., Walker, A., et al. 2004, AJ, 128, 1167
Gieren, W., Pietrzyński, G., Soszyński, I., et al. 2005, ApJ, 628, 695
Gonzalez, A., Gamba, R., Breschi, M., et al. 2023, Phys. Rev. D, 107, 084026
Götberg, Y., de Mink, S. E., Groh, J. H., et al. 2018, A&A, 615, A78
Gräfener, G., Koesterke, L., & Hamann, W. R. 2002, A&A, 387, 244
Gray, R. O., & Corbally, C., Jr 2009, Stellar Spectral Classification (Princeton: Princeton University Press)
Gross, J., Williams, B. F., Pannuti, T. G., et al. 2019, ApJ, 877, 15
Guillochon, J., & Ramirez-Ruiz, E. 2013, ApJ, 767, 25
Hainich, R., Rühling, U., Todt, H., et al. 2014, A&A, 565, A27
Hamann, W. R., & Gräfener, G. 2003, A&A, 410, 993
Helou, G., Roussel, H., Appleton, P., et al. 2004, ApJS, 154, 253
HI4PI Collaboration (Ben Bekhti, N., et al.) 2016, A&A, 594, A116
Israel, G. L., & Stella, L. 1996, ApJ, 468, 369
Israel, G. L., Esposito, P., Rodríguez Castillo, G. A., & Sidoli, L. 2016, MNRAS, 462, 4371
Israel, G. L., Belfiore, A., Stella, L., et al. 2017, Science, 355, 817
Johnson, H. L. 1966, ARA&A, 4, 193
Kaaret, P., Feng, H., & Roberts, T. P. 2017, ARA&A, 55, 303
Kato, S. 1990, PASJ, 42, 99
Knigge, C. 2006, MNRAS, 373, 484
Kobulnicky, H. A., Nordsieck, K. H., Burgh, E. B., et al. 2003, in Instrument Design and Performance for Optical/Infrared Ground-based Telescopes, eds. M. Iye, & A. F. M. Moorwood, SPIE Conf. Ser., 4841, 1634
Laycock, S. G. T., Maccarone, T. J., & Christodoulou, D. M. 2015, MNRAS, 452, L31
Leitherer, C., Schaerer, D., Goldader, J. D., et al. 1999, ApJS, 123, 3
Leitherer, C., Ekström, S., Meynet, G., et al. 2014, ApJS, 212, 14
Liedahl, D. A., Osterheld, A. L., & Goldstein, W. H. 1995, ApJ, 438, L115
Lindegren, L., Bastian, U., Biermann, M., et al. 2021, A&A, 649, A4
Liu, J.-F., Bregman, J. N., Bai, Y., Justham, S., & Crowther, P. 2013, Nature, 503, 500
Lorenzin, A., & Zampieri, L. 2009, MNRAS, 394, 1588
Lyons, L. 2008, Ann. Appl. Stat., 2, 887
Maliszewski, K., Giersz, M., Gondek-Rosinska, D., Askar, A., & Hypki, A. 2022, MNRAS, 514, 5879
McLeod, A. F., Dale, J. E., Ginsburg, A., et al. 2015, MNRAS, 450, 1057
McLeod, A. F., Kruijssen, J. M. D., Weisz, D. R., et al. 2020, ApJ, 891, 25
Mennickent, R. E., Pietrzyński, G., & Gieren, W. 2004, MNRAS, 350, 679
Mewe, R., Gronenschild, E. H. B. M., & van den Oord, G. H. J. 1985, A&AS, 62, 197
Mewe, R., Lemen, J. R., & van den Oord, G. H. J. 1986, A&AS, 65, 511
Miller, J. M., Kaastra, J. S., Miller, M. C., et al. 2015, Nature, 526, 542
Muñoz-Mateos, J. C., Gil de Paz, A., Boissier, S., et al. 2007, ApJ, 658, 1006
O'Donoghue, D., Buckley, D. A. H., Balona, L. A., et al. 2006, MNRAS, 372, 151
Page, M. J., Brindle, C., Talavera, A., et al. 2012, MNRAS, 426, 903
Pannuti, T. G., Duric, N., Lacey, C. K., et al. 2000, ApJ, 544, 780
Pasham, D. R., Remillard, R. A., Fragile, P. C., et al. 2019, Science, 363, 531
Payne, J. L., Filipović, M. D., Pannuti, T. G., et al. 2004, A&A, 425, 443
Peña, M., Reyes-Pérez, J., Hernández-Martínez, L., & Pérez-Guillén, M. 2012, A&A, 547, A78
Phinney, E. S. 1989, in The Center of the Galaxy, ed. M. Morris, IAU Symp., 136, 543
Pietrzyński, G., Gieren, W., Fouqué, P., & Pont, F. 2001, A&A, 371, 497
Pietrzyński, G., Gieren, W., Fouqué, P., & Pont, F. 2002, AJ, 123, 789
Pinto, C., & Walton, D. J. 2023, ArXiv e-prints [arXiv:2302.00006]
Pinto, C., Soria, R., Walton, D. J., et al. 2021, MNRAS, 505, 5058
Qiu, Y., Soria, R., Wang, S., et al. 2019, ApJ, 877, 57
Ramsay, G., Schreiber, M. R., Gänsicke, B. T., & Wheatley, P. J. 2017, A&A, 604, A107
Raymond, J. C., & Smith, B. W. 1977, ApJS, 35, 419
Read, A. M., & Pietsch, W. 2001, A&A, 373, 473
Rees, M. J. 1988, Nature, 333, 523
Rizzuto, F. P., Naab, T., Spurzem, R., et al. 2021, MNRAS, 501, 5257
Rizzuto, F. P., Naab, T., Spurzem, R., et al. 2022, MNRAS, 512, 884
Roussel, H., Gil de Paz, A., Seibert, M., et al. 2005, ApJ, 632, 227
Sadowski, A. 2011, PhD Thesis, Nicolaus Copernicus Astronomical Center, Polish Academy of Sciences, Poland
Sander, A. A. C., & Vink, J. S. 2020, MNRAS, 499, 873
Sander, A., Todt, H., Hainich, R., & Hamann, W. R. 2014, A&A, 563, A89
Sander, A., Shenar, T., Hainich, R., et al. 2015, A&A, 577, A13
Sander, A. A. C., Lefever, R. R., Poniatowski, L. G., et al. 2023, A&A, 670, A83
Schild, H., & Testor, G. 1992, A&A, 266, 145
Schild, H., Crowther, P. A., Abbott, J. B., & Schmutz, W. 2003, A&A, 397, 859
Schlafly, E. F., & Finkbeiner, D. P. 2011, ApJ, 737, 103
Sidoli, L., Esposito, P., Motta, S. E., Israel, G. L., & Rodríguez Castillo, G. A. 2016, MNRAS, 460, 3637
Sidoli, L., Israel, G. L., Esposito, P., Rodríguez Castillo, G. A., & Postnov, K. 2017, MNRAS, 469, 3056
Smith, R. K., Brickhouse, N. S., Liedahl, D. A., & Raymond, J. C. 2001, ApJ, 556, L91
Soria, R., & Kong, A. 2016, MNRAS, 456, 1837
Starrfield, S., Timmes, F. X., Hix, W. R., et al. 2004, ApJ, 612, L53
Straub, O., Bursa, M., Sądowski, A., et al. 2011, A&A, 533, A67
Tiengo, A., Esposito, P., Toscani, M., et al. 2022, A&A, 661, A68
Toribio san Cipriano, L., García-Rojas, J., Esteban, C., Bresolin, F., & Peimbert, M. 2016, MNRAS, 458, 1866
Urquhart, R., & Soria, R. 2016, MNRAS, 456, 1859
Urquhart, R., Soria, R., Pakull, M. W., et al. 2019, MNRAS, 482, 2389
van den Heuvel, E. P. J., Bhattacharya, D., Nomoto, K., & Rappaport, S. A. 1992, A&A, 262, 97
van den Heuvel, E. P. J., Portegies Zwart, S. F., & de Mink, S. E. 2017, MNRAS, 471, 4256
Verner, D. A., Ferland, G. J., Korista, K. T., & Yakovlev, D. G. 1996, ApJ, 465, 487
Walton, D. J., Mackenzie, A. D. A., Gully, H., et al. 2022, MNRAS, 509, 1587
Warner, B. 1987, MNRAS, 227, 23
Wen, S., Jonker, P. G., Stone, N. C., Zabludoff, A. I., & Cao, Z. 2022, ApJ, 933, 31
Williams, R. 2016, J. Phys. Conf. Ser., 728, 042001
Williams, R. E., Phillips, M. M., & Hamuy, M. 1994, ApJS, 90, 297
Wilms, J., Allen, A., & McCray, R. 2000, ApJ, 542, 914
Yershov, V. N. 2014, Ap&SS, 354, 97

Appendix A: X-ray observations

The journal of the X-ray observations is given in Table A.1.

Table A.1. Journal of the *Chandra*, *XMM-Newton* and *Swift*/XRT observations used in this work. Errors are at 1σ and upper limits at 3σ. The corresponding fluxes are shown in Fig. 3.

Instrument	Obs.ID	Date	Exposure (ks)	Rate (counts s^{-1})
XMM-Newton(pn)	0112800201	2000-12-26/27	30.0	$< 2.64 \times 10^{-3}$
XMM-Newton(pn)	0112800101	2001-01-01/02	40.0	$< 8.73 \times 10^{-4}$
XMM-Newton(pn)	0305860401	2005-05-22	28.1	$< 2.76 \times 10^{-3}$
XMM-Newton(MOS)	0305860301	2005-11-25	36.0	$< 7.23 \times 10^{-4}$
XRT	00035866001	2006-09-05	0.8	$< 2.27 \times 10^{-2}$
XRT	00035866002	2006-11-01	0.6	$< 1.98 \times 10^{-2}$
XRT	00035866003	2006-11-07	1.8	$< 6.19 \times 10^{-3}$
XRT	00030848001	2006-12-27	2.0	$< 5.58 \times 10^{-3}$
XRT	00030848002	2006-12-29	9.9	$< 1.05 \times 10^{-3}$
XRT	00030848003	2006-12-30	9.6	$< 1.07 \times 10^{-3}$
XRT	00030848004	2006-12-31	9.4	$< 1.13 \times 10^{-3}$
XRT	00030848005	2007-01-01	9.2	$< 1.60 \times 10^{-3}$
XRT	00030848006	2007-01-02	7.7	$< 1.33 \times 10^{-3}$
XRT	00030848007	2007-01-03	8.8	$< 1.21 \times 10^{-3}$
XRT	00030848008	2007-01-04	2.3	$< 4.90 \times 10^{-3}$
XRT	00030848009	2007-01-05	5.0	$< 2.65 \times 10^{-3}$
XRT	00030848010	2007-01-06	8.7	$< 1.37 \times 10^{-3}$
XRT	00030848011	2007-01-07	7.0	$< 1.76 \times 10^{-3}$
XRT	00030848012	2007-01-08	3.8	$< 4.67 \times 10^{-3}$
XRT	00035866004	2007-01-28/29	1.7	$< 6.65 \times 10^{-3}$
XRT	00031210001	2008-05-20	6.1	$< 2.14 \times 10^{-3}$
XRT	00031210002	2008-05-25	7.1	$< 1.85 \times 10^{-3}$
XRT	00031210003	2008-06-04	6.9	$< 1.88 \times 10^{-3}$
XRT	00031210004	2008-06-19	8.0	$< 2.77 \times 10^{-3}$
XRT	00031210005	2008-08-14	2.1	$< 6.52 \times 10^{-3}$
XRT	00031210006	2008-08-15	2.2	$< 6.00 \times 10^{-3}$
XRT	00031210007	2008-08-26	4.7	$< 3.97 \times 10^{-3}$
XRT	00031210008	2008-10-15	2.1	$< 5.28 \times 10^{-3}$
XRT	00031210009	2008-10-16	1.6	$< 8.56 \times 10^{-3}$
XRT	00031726001	2010-05-24/26	6.6	$< 2.01 \times 10^{-3}$
XRT	00031726002	2010-05-26	2.7	$< 5.19 \times 10^{-3}$
XMM-Newton(pn)	0656780401	2010-05-28	18.1	$< 4.42 \times 10^{-3}$
XRT	00031726003	2010-05-28	3.2	$< 4.27 \times 10^{-3}$
XRT	00031726004	2010-05-30	3.2	$< 4.02 \times 10^{-3}$
XRT	00031726005	2010-06-01	3.9	$< 4.68 \times 10^{-3}$
XRT	00031726006	2010-06-03	3.0	$< 4.38 \times 10^{-3}$
XRT	00031726007	2010-06-05	4.5	$< 2.89 \times 10^{-3}$
XRT	00031726008	2010-06-07	4.1	$< 3.16 \times 10^{-3}$
XRT	00031726009	2010-06-09	4.0	$< 3.28 \times 10^{-3}$
XRT	00031726010	2010-06-11	3.8	$< 3.57 \times 10^{-3}$
XRT	00031726011	2010-06-16	4.0	$< 4.49 \times 10^{-3}$
XRT	00031726012	2010-06-17	4.2	$< 3.19 \times 10^{-3}$
XRT	00031726013	2010-06-18	4.2	$< 3.23 \times 10^{-3}$
XRT	00031726015	2010-06-21	2.2	$< 6.01 \times 10^{-3}$
XRT	00031726016	2010-06-25	1.3	$< 1.07 \times 10^{-2}$
XRT	00031726017	2010-07-01	4.0	$< 3.36 \times 10^{-3}$
Chandra	12238	2010-09-24/25	63.0	$< 1.7 \times 10^{-4}$
XRT	00031726018	2010-09-26	2.3	$< 7.93 \times 10^{-3}$

Table A.1. Continued.

Instrument	Obs.ID	Date	Exposure (ks)	Rate (counts s^{-1})
XRT	00031726019	2010-09-27	3.5	$< 3.76 \times 10^{-3}$
XRT	00031726020	2010-09-28	4.3	$< 3.08 \times 10^{-3}$
XRT	00049834001	2013-11-27	0.5	$< 2.6 \times 10^{-2}$
Chandra	16028	2014-05-16/17	64.2	$< 9.3 \times 10^{-5}$
Chandra	16029	2014-11-17/18	61.3	$(9.0 \pm 0.4) \times 10^{-3}$
XRT	00049834002	2016-04-14	0.6	$< 2.38 \times 10^{-2}$
XRT	00049834003	2016-04-20	0.5	$< 2.83 \times 10^{-2}$
XRT	00049834005	2016-04-24/25	2.9	$< 6.28 \times 10^{-3}$
XMM-Newton(pn)	0791010101	2016-12-17/18	102.6	$< 1.72 \times 10^{-3}$
XMM-Newton(pn)	0791010301	2016-12-19/20	47.5	$< 3.90 \times 10^{-3}$
XRT	00049834006	2017-04-13	1.1	$< 1.26 \times 10^{-2}$
XRT	00049834007	2017-04-14/15	2.5	$< 5.23 \times 10^{-3}$
XRT	00049834008	2017-04-16/7	1.9	$< 7.25 \times 10^{-3}$
XRT	00049834009	2017-04-21	0.5	$< 2.63 \times 10^{-2}$
XRT	00049834010	2017-04-24	5.2	$< 2.51 \times 10^{-3}$
XRT	00049834012	2017-07-02	1.3	$< 8.76 \times 10^{-3}$
XRT	00049834013	2017-07-06	1.9	$< 7.02 \times 10^{-3}$
XRT	00049834014	2017-07-12	1.8	$< 7.48 \times 10^{-3}$
XRT	00049834015	2018-01-25	5.0	$< 2.25 \times 10^{-3}$
XRT	00088651001	2018-01-31	5.1	$< 2.17 \times 10^{-3}$
XRT	00049834016	2018-02-07	4.6	$< 3.91 \times 10^{-3}$
XRT	00049834017	2018-02-14	4.8	$< 2.83 \times 10^{-3}$
XRT	00049834018	2018-04-12	0.3	$< 4.42 \times 10^{-2}$
XRT	00049834019	2018-04-13/14	3.5	$< 3.87 \times 10^{-3}$
XRT	00049834020	2018-04-18	2.6	$< 5.22 \times 10^{-3}$
XRT	00049834021	2018-04-25	6.1	$< 2.19 \times 10^{-3}$
XRT	00049834022	2018-04-26	5.2	$< 2.55 \times 10^{-3}$
XRT	00049834023	2018-04-27	4.9	$< 3.70 \times 10^{-3}$
XRT	00049834024	2018-04-28	4.8	$< 2.75 \times 10^{-3}$
XRT	00049834025	2018-04-29	4.9	$< 3.66 \times 10^{-3}$
XRT	00049834026	2018-04-30	5.0	$< 2.70 \times 10^{-3}$
XRT	00049834027	2018-05-01	4.7	$< 3.71 \times 10^{-3}$
XRT	00049834028	2018-05-02	5.0	$< 3.58 \times 10^{-3}$
XRT	00049834029	2018-05-03	4.9	$< 2.83 \times 10^{-3}$
XRT	00049834030	2018-05-04	4.8	$< 2.71 \times 10^{-3}$
XRT	00049834031	2018-05-05	1.5	$< 9.21 \times 10^{-3}$
XRT	00049834032	2018-05-06	4.5	$< 5.00 \times 10^{-3}$
XRT	00049834033	2018-05-07	3.2	$< 4.25 \times 10^{-3}$
XRT	00049834034	2018-05-08	6.2	$< 3.52 \times 10^{-3}$
XRT	00049834035	2018-05-11	4.9	$< 3.72 \times 10^{-3}$
XRT	00049834036	2018-05-14	4.9	$< 2.78 \times 10^{-3}$
XRT	00049834037	2018-05-17	4.8	$< 2.76 \times 10^{-3}$
XRT	00049834038	2018-05-20	4.7	$< 2.95 \times 10^{-3}$

Table A.1. Continued.

Instrument	Obs.ID	Date	Exposure (ks)	Rate (counts s^{-1})
XRT	00049834039	2018-05-23	4.9	$< 3.58 \times 10^{-3}$
XRT	00049834040	2018-05-26	4.8	$< 2.80 \times 10^{-3}$
XRT	00049834041	2018-05-29	4.7	$< 2.79 \times 10^{-3}$
XRT	00049834043	2018-06-01	4.9	$< 2.80 \times 10^{-3}$
XRT	00049834044	2018-06-07	5.2	$< 2.55 \times 10^{-3}$
XRT	00049834045	2018-06-10	4.7	$< 2.86 \times 10^{-3}$
XRT	00049834046	2018-06-13	4.9	$< 2.68 \times 10^{-3}$
XRT	00049834047	2018-06-16	4.7	$< 2.87 \times 10^{-3}$
XRT	00049834048	2018-06-19	4.7	$< 2.85 \times 10^{-3}$
XRT	00049834049	2018-06-28	3.8	$< 3.60 \times 10^{-3}$
XRT	00049834050	2018-07-03	4.3	$< 3.20 \times 10^{-3}$
XRT	00049834051	2018-07-08	4.4	$< 2.53 \times 10^{-3}$
XRT	00049834052	2018-07-13	3.7	$< 4.83 \times 10^{-3}$
XRT	00049834053	2018-07-18	3.6	$< 5.12 \times 10^{-3}$
XRT	00049834054	2018-07-23	4.3	$< 3.09 \times 10^{-3}$
XRT	00049834055	2018-07-28	3.8	$< 3.64 \times 10^{-3}$
XRT	00049834056	2018-08-02	3.9	$< 3.45 \times 10^{-3}$
XRT	00049834057	2018-08-07	4.0	$< 3.38 \times 10^{-3}$
XRT	00049834058	2018-08-12	4.0	$< 3.38 \times 10^{-3}$
XRT	00049834059	2018-08-29	3.6	$(1.9 \pm 1.0) \times 10^{-3}$
XRT	00049834060	2018-09-05	3.8	$< 3.52 \times 10^{-3}$
XRT	00049834061	2018-09-12	4.5	$< 3.02 \times 10^{-3}$
XRT	00049834063	2018-09-23	4.8	$< 2.73 \times 10^{-3}$
XRT	00049834064	2018-09-26	4.6	$< 2.87 \times 10^{-3}$
XRT	00049834065	2018-10-03	4.7	$< 2.76 \times 10^{-3}$
XRT	00088810002	2018-10-07	4.9	$< 2.66 \times 10^{-3}$
XRT	00049834066	2018-10-10	2.1	$< 6.39 \times 10^{-3}$
XRT	00049834067	2018-10-14	2.9	$< 4.40 \times 10^{-3}$
XRT	00049834068	2018-10-17	4.7	$< 2.27 \times 10^{-3}$
XRT	00049834070	2018-11-18	1.0	$< 1.17 \times 10^{-2}$
XRT	00049834071	2018-11-25	0.4	$< 3.41 \times 10^{-2}$
XRT	00049834072	2018-11-28	0.6	$< 2.31 \times 10^{-2}$
XRT	00049834073	2018-12-02	1.0	$< 1.43 \times 10^{-2}$
XRT	00049834074	2018-12-09	1.1	$< 1.18 \times 10^{-2}$
XRT	00049834075	2018-12-16	1.0	$< 1.41 \times 10^{-2}$
XRT	00049834076	2018-12-23	0.6	$< 1.79 \times 10^{-2}$
XRT	00049834077	2018-12-30	0.9	$< 1.46 \times 10^{-2}$
XRT	00049834078	2019-01-06	0.3	$< 4.21 \times 10^{-2}$
XRT	00049834080	2019-01-13	2.0	$< 6.83 \times 10^{-3}$
XRT	00049834081	2019-01-20	2.0	$(3.4 \pm 1.8) \times 10^{-3}$
XRT	00049834082	2019-01-27	1.8	$< 1.02 \times 10^{-2}$
XRT	00049834083	2019-02-03	1.8	$< 7.68 \times 10^{-3}$
XRT	00049834084	2019-02-10	2.0	$< 6.95 \times 10^{-3}$
XRT	00049834085	2019-04-13	2.1	$< 6.56 \times 10^{-3}$
XRT	00049834086	2019-04-20	2.5	$< 5.37 \times 10^{-3}$
XRT	00049834087	2019-04-27	0.4	$< 3.73 \times 10^{-2}$
XRT	00049834088	2019-05-04	2.3	$< 5.81 \times 10^{-3}$
XRT	00049834089	2019-05-11	2.1	$< 7.56 \times 10^{-3}$

Table A.1. Continued.

Instrument	Obs.ID	Date	Exposure (ks)	Rate (counts s^{-1})
XRT	00031726021	2019-09-20	1.9	$< 7.16 \times 10^{-3}$
XRT	00012017001	2019-09-26	2.5	$< 5.45 \times 10^{-3}$
XRT	00012017002	2019-09-26	3.0	$< 4.48 \times 10^{-3}$
XRT	00012017004	2019-09-27	3.1	$< 4.43 \times 10^{-3}$
XRT	00012160001	2019-11-11	0.8	$< 1.75 \times 10^{-2}$
XRT	00012160002	2019-11-14	0.8	$< 2.49 \times 10^{-2}$
XRT	00012160003	2019-11-16	1.2	$< 1.94 \times 10^{-2}$
XRT	00095672001	2020-04-16	3.7	$(2.8 \pm 1.3) \times 10^{-3}$
Chandra	22375	2020-04-26/27	47.4	$(1.0 \pm 0.2) \times 10^{-3}$
XRT	00095672002	2020-04-30	3.1	$< 4.36 \times 10^{-3}$
XRT	00095672003	2020-05-14	3.8	$< 3.52 \times 10^{-3}$
XRT	00095672004	2020-05-28	3.3	$< 4.01 \times 10^{-3}$
XRT	00095672005	2020-06-11	3.6	$< 3.73 \times 10^{-3}$
XRT	00095672006	2020-06-25	3.3	$< 3.53 \times 10^{-3}$
XRT	00095672007	2020-07-09	3.7	$< 3.06 \times 10^{-3}$
XRT	00095672008	2020-07-23	3.8	$< 3.71 \times 10^{-3}$
XRT	00095672009	2020-08-06	2.9	$< 4.67 \times 10^{-3}$
XRT	00095672010	2020-08-20	3.1	$< 5.98 \times 10^{-3}$
XRT	00095672011	2020-09-03	3.8	$< 3.50 \times 10^{-3}$
XRT	00095672012	2020-09-17	3.9	$(5.1 \pm 1.7) \times 10^{-3}$
XRT	00095672013	2020-10-01	3.2	$< 5.79 \times 10^{-3}$
XRT	00095672014	2020-10-15	3.1	$< 4.38 \times 10^{-3}$
XRT	00095672015	2020-10-29	3.9	$< 3.40 \times 10^{-3}$
XRT	00095672016	2020-11-12	3.9	$< 2.79 \times 10^{-3}$
XRT	00095672017	2020-11-26	3.9	$< 2.81 \times 10^{-3}$
XRT	00095672018	2020-12-10	2.3	$< 5.54 \times 10^{-3}$
XRT	00095672019	2020-12-15	1.6	$< 1.08 \times 10^{-2}$
XRT	00095672020	2020-12-24	3.8	$< 5.87 \times 10^{-3}$
XRT	00095672021	2021-01-07	3.7	$< 2.92 \times 10^{-3}$
XRT	00095672022	2021-01-21	3.5	$< 3.14 \times 10^{-3}$
XRT	00095672023	2021-02-04	3.9	$< 3.38 \times 10^{-3}$
XRT	00031726022	2021-10-23	1.4	$< 9.29 \times 10^{-3}$
XRT	00031726023	2021-11-23	2.1	$< 5.11 \times 10^{-3}$
XRT	00031726024	2021-12-22	0.7	$< 1.99 \times 10^{-2}$
XRT	00031726025	2021-12-28	1.8	$< 8.58 \times 10^{-3}$
XRT	00031726028	2022-04-13	4.7	$< 2.78 \times 10^{-3}$
XRT	00031726029	2022-10-01	2.1	$< 7.43 \times 10^{-3}$
XRT	00031726030	2022-10-18	0.2	$< 6.80 \times 10^{-2}$
XRT	00031726031	2022-10-29	1.5	$< 7.51 \times 10^{-3}$
XRT	00031726033	2022-11-26	1.5	$< 8.98 \times 10^{-3}$
XRT	00031726034	2022-12-10	1.6	$< 1.13 \times 10^{-2}$

Appendix B: SALT spectrum

The parameters of the emission lines in the optical SALT spectrum are reported in Table B.1. The lower-resolution spectrum (PG0300) is shown in Fig. B.1.

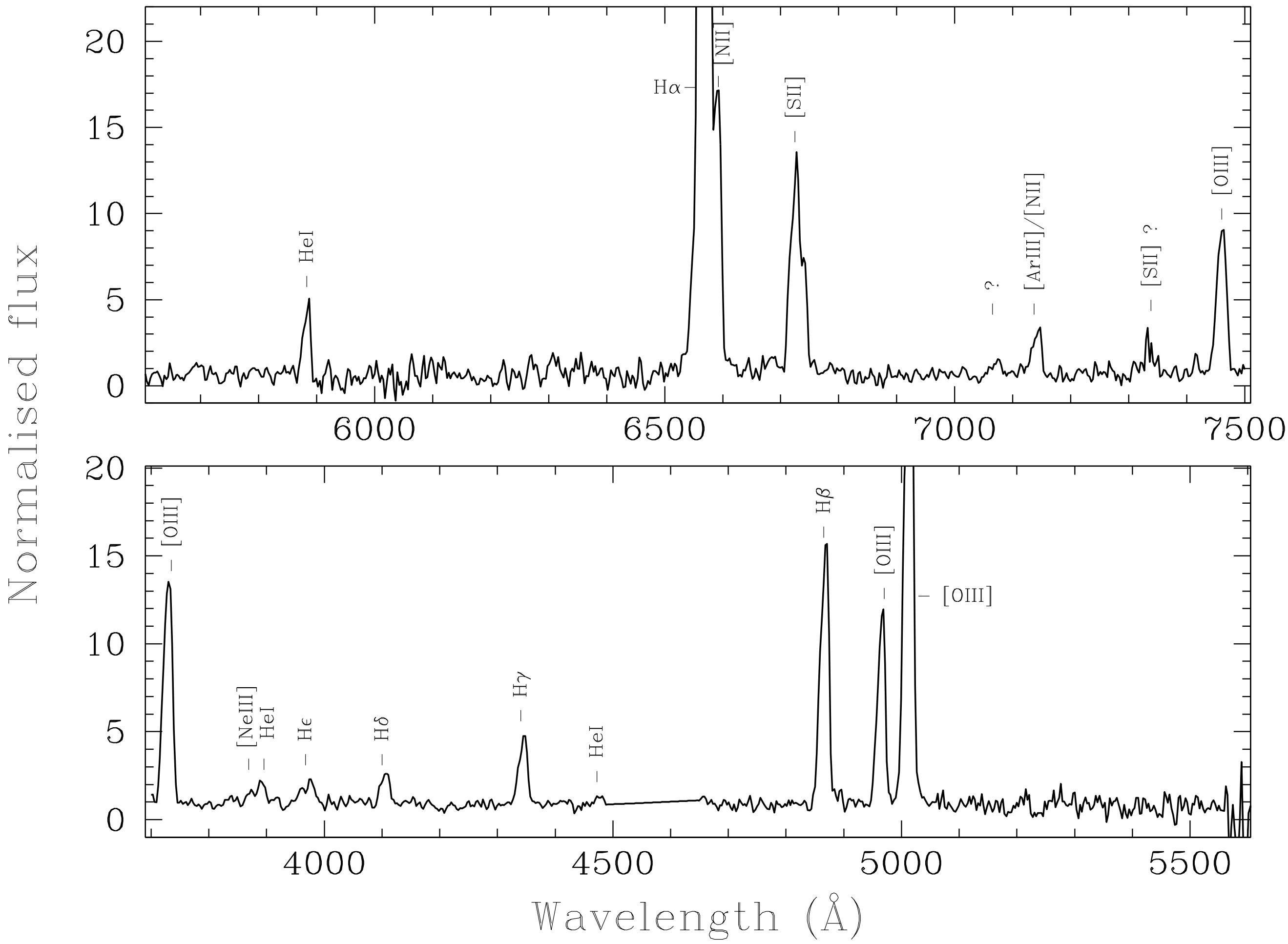

Fig. B.1. SALT spectrum (PG0300) of J0054. The lines labelled with a question mark are better identified and resolved in the PG0900 spectrum (Fig. 7).

Table B.1. Parameters of emission lines in the two SALT spectra.

Element	λ^1 (Å)	FWHM (Å)	EQW (Å)	V^2_{rad} (km/s)	Notes
			02 December 2019		
[OII]	3729.1 ± 0.2	17.4 ± 0.5	332 ± 13	121 ± 17	blend of 3726 − 3729 Å
[NeIII]	3872.3 ± 0.1	12.1 ± 3.7	9.7 ± 3.7	252 ± 12	blended with HeI 3888.64 Å
HeI	3891.3 ± 0.9	14.0 ± 2.2	21.9 ± 4.1	182 ± 66	blended with [NeIII] 3868.75 Å
[OIII]	3960.0 ± 1.6	11.7 ± 3.8	12.6 ± 6.0	−143 ± 12	uncertain identification
H_ϵ	3976.8 ± 1.1	13.7 ± 2.7	24.0 ± 8.2	483 ± 83	blended possibly with [OIII] 3961.59 Å
H_δ	4105.8 ± 0.6	16.6 ± 1.5	39.5 ± 4.8	275 ± 47	
H_γ	4344.8 ± 0.3	17.1 ± 0.6	99.6 ± 4.9	273 ± 18	
HeI	4477.03 ± 0.01	36.74 ± 0.01	5.0 ± 2.0	349.37 ± 0.01	double-peaked, manually measured
H_β	4867.0 ± 0.3	16.7 ± 0.7	330 ± 17	328 ± 16	with additional red-component
[OIII]	4965.5 ± 0.3	15.2 ± 0.8	240 ± 18	375 ± 19	
[OIII]	5013.3 ± 0.3	16.0 ± 0.9	702 ± 51	365 ± 20	
HeI	5883.4 ± 0.6	13.6 ± 1.4	113 ± 15	376 ± 29	
H_α	6569.7 ± 0.3	17.5 ± 0.7	1731 ± 89	294 ± 12	blended with [NII] 6548 Å, and partially with 6584 Å
[NII]	6593.4 ± 0.2	16.1 ± 0.6	8.6 ± 3.9	426.9 ± 7.3	blended with H_α
[SII]	6726.0 ± 0.3	20.5 ± 0.8	288 ± 14	402 ± 14	blended with [SII] 6731 Å
[NII]	7141.5 ± 0.6	18.3 ± 1.4	95.8 ± 9.6	88 ± 24	uncertain identification or [ArIII]7136 Å
[ArIII]				208 ± 24	if [ArIII]
[OIII]	7459.9 ± 0.3	18.3 ± 0.7	223 ± 11	159 ± 11	
			15 December 2019		
H_γ	4344.35 ± 0.08	5.4 ± 0.2	64.0 ± 3.1	242.5 ± 5.7	
H_β	4865.0 ± 0.1	5.6 ± 0.3	180 ± 11	206.0 ± 6.5	
[OIII]	4963.0 ± 0.1	5.5 ± 0.4	106.7 ± 9.3	225.1 ± 9.1	
[OIII]	5011.0 ± 0.5	5.4 ± 0.1	325.9 ± 9.4	224 ± 29	
HeI	5879.9 ± 0.1	5.5 ± 0.3	92.3 ± 7.4	196.0 ± 6.9	
[NII]	6553.4 ± 0.8	9.6 ± 7.2	77.3 ± 7.5	223 ± 38	
H_α	6567.73 ± 0.08	5.5 ± 0.2	1264 ± 57	200.9 ± 3.6	
[NII]	6588.3 ± 0.7	5.8 ± 1.6	163 ± 60	200 ± 30	
HeI	6683.6 ± 0.2	4.9 ± 0.5	15.0 ± 2.0	220.4 ± 9.0	
[SII]	6721.3 ± 0.1	5.9 ± 0.2	181.5 ± 9.6	193.9 ± 4.3	
[SII]	6735.6 ± 0.1	6.1 ± 0.3	132.0 ± 9.8	190.4 ± 6.2	
[ArIII]	7141.1 ± 0.1	4.9 ± 0.4	43.3 ± 4.1	192.9 ± 6.9	

Notes. All parameters were measured by Gaussian fits unless otherwise noted. [1] Line wavelength in Å. [2] Radial velocity heliocentric corrected.